remote sensing

MDPI

Article

UAV-Based Multiple Sensors for Enhanced Data Fusion and Nitrogen Monitoring in Winter Wheat Across Growth Seasons

Jingjing Wang [1], Wentao Wang [1], Suyi Liu [1], Xin Hui [1], Haohui Zhang [1], Haijun Yan [1,2,*] and Wouter H. Maes [3]

[1] College of Water Resources and Civil Engineering, China Agricultural University, Beijing 100083, China; wangjingjing9@cau.edu.cn (J.W.); wwt@cau.edu.cn (W.W.); s20223091918@cau.edu.cn (S.L.); xinhui@nwafu.edu.cn (X.H.); bs20223090744@cau.edu.cn (H.Z.)
[2] State Key Laboratory of Efficient Utilization of Agricultural Water Resources, China Agricultural University, Beijing 100083, China
[3] UAV Research Centre, Department of Plants and Crops, Ghent University, 9000 Ghent, Belgium; wouter.maes@ugent.be
* Correspondence: yanhj@cau.edu.cn

Abstract: Unmanned aerial vehicles (UAVs) equipped with multi-sensor remote sensing technologies provide an efficient approach for mapping spatial and temporal variations in vegetation traits, enabling advancements in precision monitoring and modeling. This study's objective was to analyze UAV multiple sensors' performance in monitoring winter wheat chlorophyll content (SPAD), plant nitrogen accumulation (PNA), and N nutrition index (NNI). A two-year field experiment with five N fertilizer treatments was carried out. The color indices (CIs, from RGB sensors), vegetation indices (VIs, from multispectral sensors), and temperature indices (TIs, from thermal sensors) were derived from the collected images. XGBoost (extreme gradient boosting) was applied to develop the models, using 2021 data for training and 2022 data for testing. The excess green minus excess red index, red green ratio index, and hue (from CIs), and green normalized difference vegetation index, normalized difference red-edge index, and normalized difference vegetation index (from VIs), showed high correlations with three N indicators. At the pre-heading stage, the best performing CIs correlated better than the VIs; this was reversed in the post-heading stage. CIs outperformed VIs in SPAD (CIs: R^2(coefficient of determination) = 0.66, VIs: R^2 = 0.61), PNA (CIs: R^2 = 0.68, VIs: R^2 = 0.64), and NNI (CIs: R^2 = 0.64, VIs: R^2 = 0.60) in the pre-heading stage, whereas VI-based models achieved slightly higher accuracies in post-heading and all stages compared to CIs. Models built with CIs + VIs significantly improved the models' performance compared to single-sensor models. Adding TIs to CIs and CIs + VIs further improved the models' performance slightly, especially at the post-heading stage, resulting in the best model performance with three sensors. These findings highlight the effectiveness of UAV systems in estimating wheat N and establish a framework for integrating RGB, multispectral, and thermal sensors to enhance model accuracy in precision vegetation monitoring.

Keywords: UAV-based remote sensing; multi-sensor integration; multispectral; RGB; thermal; vegetation monitoring; XGBoost modeling

check for updates

Academic Editor: Annamaria Castrignanò

Received: 7 December 2024
Revised: 22 January 2025
Accepted: 27 January 2025
Published: 31 January 2025

Citation: Wang, J.; Wang, W.; Liu, S.; Hui, X.; Zhang, H.; Yan, H.; Maes, W.H. UAV-Based Multiple Sensors for Enhanced Data Fusion and Nitrogen Monitoring in Winter Wheat Across Growth Seasons. *Remote Sens.* **2025**, *17*, 498. https://doi.org/10.3390/rs17030498

Copyright: © 2025 by the authors. Licensee MDPI, Basel, Switzerland. This article is an open access article distributed under the terms and conditions of the Creative Commons Attribution (CC BY) license (https://creativecommons.org/licenses/by/4.0/).

1. Introduction

Nitrogen (N) is a vital macronutrient in promoting plant growth through facilitating photosynthesis and increases both the quantity and quality of crop yields [1–3]. However, excessive N application can disturb grain filling [4], lodging [5,6], and environmental

pollution. Hence, precise crop N estimation and optimized N fertilizer management are crucial for food security and environmental protection in crop production [7,8]. Remote sensing technologies, particularly platforms based on unmanned aerial vehicles (UAVs), offer significant advantages over conventional ground-based sampling and chemical analyses in monitoring N status. UAVs provide high spatial and temporal resolution, allowing for flexible and detailed assessments during critical growth stages [9,10].

Among UAV-mounted sensors, multispectral, RGB, and thermal sensors are widely employed for crop monitoring. Multispectral sensors are commonly used due to their ability to capture reflectance across key spectral regions, including near-infrared and red-edge, which are closely associated with chlorophyll and N content [11]. While multispectral sensors dominate N estimation research, RGB sensors offer complementary advantages, including cost-effectiveness, user-friendliness, and the ability to capture high-resolution spatial and color features related to crop N levels. Furthermore, thermal sensors capture physiological responses, such as canopy temperature changes caused by N-related transpiration differences, making them a valuable addition to crop monitoring systems [12–15].

Most existing studies have focused on single sensors or partial combinations of sensors (e.g., RGB and multispectral) to evaluate their impact on N estimation accuracy. In recent years, UAVs and UAV sensor development have often allowed simultaneous measurements by combining RGB with multispectral data (e.g., the new DJI Mavic 3 Multispectral (DJI Sciences and Technologies Ltd., Shenzhen, China) platform, or the dual gimbal set-up on the DJI M300 and DJI M350 models), RGB with thermal sensors (e.g., DJI XT2 or DJI H20T), and multispectral with thermal sensors (e.g., Micasense Altum series (AgEagle, Seattle, WA, USA)). Researchers have demonstrated the effectiveness of combining multiple sensors to enhance crop N status monitoring. Xu et al. developed a novel set of modified coverage-adjusted spectral indices, calculated by integrating vegetation indices from multispectral images with vegetation coverage derived from RGB images [16]. Their findings showed that sensor data fusion significantly improved the accuracy of maize leaf N content estimation, particularly during the transition from the vegetative growth stage to the reproductive growth stage (R^2 = 0.59, RMSE = 22.02%, NRMSE = 8.37%). Furthermore, Xu et al. achieved higher accuracy in estimating rice leaf N content by integrating RGB and multispectral images compared to using multispectral images alone [17]. The combination of different feature types (including bands, vegetation indices, and gray level co-occurrence matrix features) was found to produce the best performance. The above studies are based on using RGB and multispectral images to evaluate N status, and the contribution of thermal data to the accuracy of N estimation models remains poorly explored. Some researchers have integrated multispectral and thermal sensors (Micasense RE-MX (AgEagle, Seattle, WA, USA) + Zenmuse (DJI Sciences and Technologies Ltd., Shenzhen, China)) to evaluate water stress in winter wheat and soil moisture conditions in maize [18,19]. However, these studies have not emphasized the critical role of thermal data in N estimation. Ding et al. fused multi-source remote sensing data (including RGB, multispectral, and thermal sensors) to enhance winter wheat N content prediction accuracy [20]. However, this study processed images from various sensors as separate entities, utilizing distinct spectral variables for input into varied models to assess crop N conditions, with limited exploration of data integration from multi-sensor sources. Matese and Di Gennaro described a UAV platform integrating RGB, multispectral, and thermal sensors for precision viticulture, focusing on vine vigor, water stress, and missing plant detection. However, this study did not extend the approach to nitrogen monitoring [21]. Additionally, Liu et al. demonstrated that integrating near-end fluorescence sensors with multi-source data fusion significantly improved the accuracy of N models for wheat across the entire growth period [22]. However, the large-scale application on drone platforms still needs to be explored. As such, exploring the

combination of these sensors and fully integrating them into data processing to build a simple and effective nitrogen monitoring framework is becoming increasingly important.

Consequently, this paper aims to achieve three objectives: (1) to analyze and compare the performance of UAV-mounted RGB, multispectral, and thermal sensors for N estimation, highlighting their unique strengths and stage-specific contributions across crop growth stages; (2) to assess whether the fusion of multiple sensors enhances model accuracy by capturing complementary spatial, spectral, and physiological information; and (3) to develop a unified, scalable framework for UAV-based nitrogen estimation using independent training and testing datasets to ensure precision and reliability.

2. Materials and Methods

2.1. The Experimental Design

This study was carried out at the China Agricultural University Experimental Station, located in Zhuozhou city, Hebei Province, China (Figure 1), during the 2021 and 2022 growing seasons. The site lies within a typical temperate monsoon climatic zone in a continental semi-humid region (Dwb under the Köppen classification). The annual mean precipitation is 560 mm and the soil texture is sandy (based on the USDA's soil texture triangle [23]), with the main physicochemical soil properties described in Table 1. Winter wheat (var. Nongda no. 212) was seeded on 12 October 2020 and 10 October 2021, with rows 0.15 m apart, and a seeding rate of 270 kg ha^{-1} in 2020–2021 and 330 kg ha^{-1} in 2021–2022.

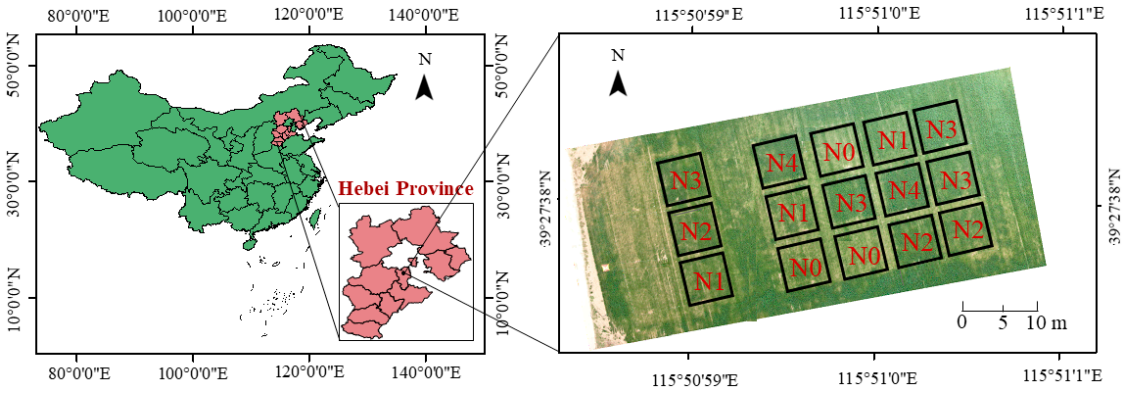


Figure 1. Treatments of the experiment (N0, N1, N2, N3, and N4 represent the nitrogen fertilization level).

Table 1. Physicochemical properties of the soil (0–80 cm) at the experimental site.

Items	Content	Annotation
pH	8.3	Determined by acid–alkali indicator method
Organic carbon (g kg^{-1})	20.2	Determined by ultraviolet–visible spectrophotometer
Available phosphorus (mg kg^{-1})	32.5	Determined by ultraviolet–visible spectrophotometer
Exchangeable potassium (mg kg^{-1})	55.0	Determined by atomic absorption spectroscopy method
Nitrate nitrogen (mg kg^{-1})	14.0	Determined by ultraviolet–visible spectrophotometer
Ammonia nitrogen (mg kg^{-1})	4.6	Determined by ultraviolet–visible spectrophotometer

Five different N application levels were set up in 2021–2022 (Table 2). All these treatments received a basic fertilization at the seeding of 54, 138, and 81 kg ha^{-1} of nitrogen, phosphorus, and potassium, respectively. This application was based on typical practices in this region. Then, five top-dressing N treatments were set up between the tillering and filling stages of winter wheat (N0–N4). The N3 treatment corresponds to the conventional

N application rate recommended by local practice. N0, N1, N2, and N4 represent 0%, 33%, 67%, and 133% of N3 (top-dressing N application), respectively. Each plot had a length and width of six meters. All plots were optimally managed, including uniform irrigation, weeding, and pesticide application.

Table 2. Winter wheat N fertilizer application rates in the experiment (kg ha^{-1}).

Year	Date	N0	N1	N2	N3	N4
2021	12 October 2020	54	54	54	54	54
	30 March 2021	0	30	60	90	120
	25 April 2021	0	30	60	90	120
	10 May 2021	0	6.7	13.3	20	26.7
	Total	54	120.7	187.3	254	320.7
2022	10 October 2021	54	54	54	54	54
	2 April 2022	0	30	60	90	120
	27 April 2022	0	30	60	90	120
	19 May 2022	0	6.7	13.3	20	26.7
	Total	54	120.7	187.3	254	320.7

2.2. UAV Platform and Image Acquisition

The DJI M300 Pro UAV (DJI, China) was employed as the platform (Figure 2). RGB images and thermal images were collected synchronously by an integrated camera (Zenmuse H20T, DJI Sciences and Technologies Ltd., Shenzhen, China). Simultaneously, 5-band multispectral images were obtained with a red-edge multispectral camera (MicaSense Red-Edge MX, AgEagle, Seattle, WA, USA). The specific parameters are given in Table 3.

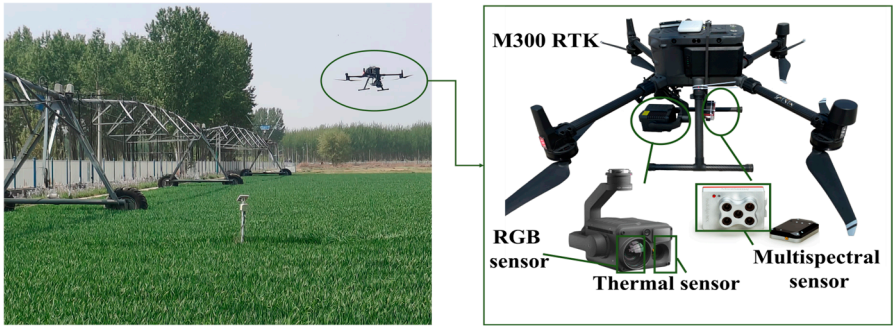


Figure 2. Unmanned aerial vehicle remote sensing platform and sensors.

Table 3. Parameters of the RGB, thermal, and multispectral sensors.

Parameters	RGB	Thermal	Multispectral
Spectral band	blue (450 nm), green (520 nm), and red (660 nm)	8–14 μm	blue (465–485 nm), green (550–570 nm), red (663–673 nm), red-edge (712–722 nm), and near-infrared (820–860 nm)
Resolution (pixels)	4050 × 3040	640 × 512	1280 × 960
Focal length (mm)	4.5	13.5	5.5
Ground sampling distance at 50 m flight height (cm)	1.0	4.5	3.5

Flights were conducted under clear sky and calm wind conditions. The images were collected six times in 2021 and five times in 2022 between 11:00 and 13:00, as shown in Table 4. All flight operations were planned using the DJI Pilot app (DJI, China), with image

acquisition based on a 75% forward and 75% lateral overlap for thermal images. The UAV flew at an altitude of 50 m, maintaining a speed of 2.1 m s^{-1}.

Table 4. Dates and growth stages of UAV data collection.

Year	Dates and Growth Stages
2021	6 April (Tillering), 22 April (Jointing), 30 April (Booting), 7 May (Heading), 11 May (Flowering), 18 May (Filling)
2022	8 April (Tillering), 15 April (Jointing), 25 April (Booting), 4 May (Heading), 14 May (Filling)

2.3. Image Data Processing

2.3.1. Image Processing

The raw images were imported into Pix4D Mapper 4.4 to create ortho-mosaic images [24]. All ortho-mosaics were processed in QGIS 3.22 and assigned to various sampling plots. The *ExG* (Table A1) was applied to isolate vegetation pixels of RGB and thermal images, by converting the ExG map into a binary image using Otsu's thresholding method (OTSU) [25] to remove the soil background. *NDVI* map (Table A2) was used to isolate vegetation pixels of multispectral images (Figure 3).

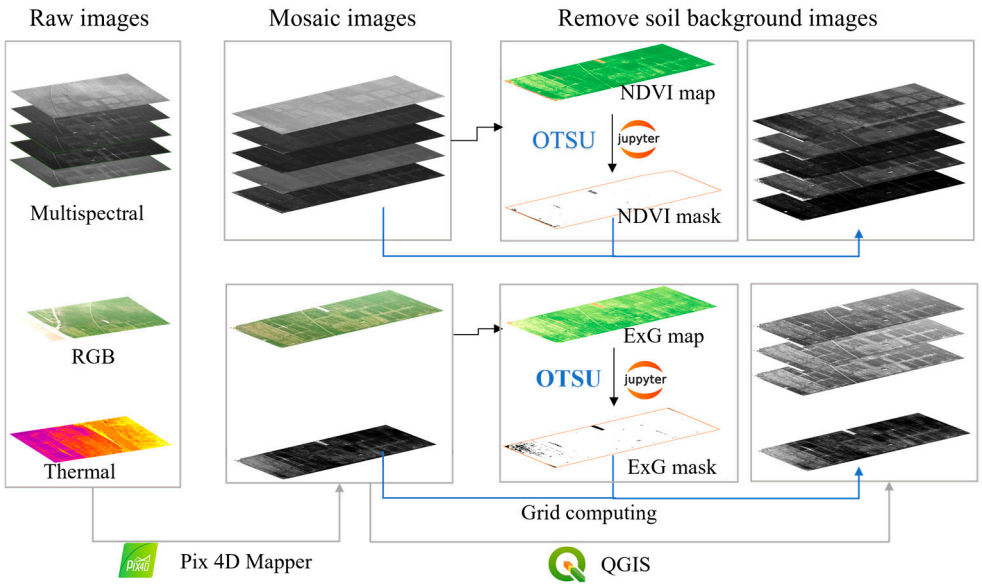


Figure 3. The data processing flow of remote sensing images.

2.3.2. Calculation of Color Indices, Vegetation Indices, and Thermal Indices

In total, fourteen color indices (CIs) were calculated from the RGB ortho mosaics (Table A1), using the RGB color space [26–35]. In addition, thirteen additional indices were calculated after conversion to other color spaces based on the formulas (Table A1) [36,37].

Eighteen vegetation indices (VIs) were derived from the multispectral data and utilized to build N prediction models for winter wheat (Table A2) [38–54].

Two thermal indices (TIs) were derived from the thermal data. Brightness temperature (T_{br}, K) was calculated using DJI Thermal SDK 1.2 software, which applied atmospheric correction based on air temperature (T_a, K), relative humidity (*RH*, %), and flight altitude (m). T_a and *RH* were measured at the experimental site using a HOBO U30 weather station

(Onset Computer Co., Bourne, MA, USA). Surface temperature (T_s, K) was then calculated using Equations (1) and (2) [55,56]:

$$T_s = \sqrt[4]{\frac{T_{br}^4 - (1 - \varepsilon) \times T_{bg}^4}{\varepsilon}} \quad (1)$$

$$T_{bg} = \sqrt[4]{0.7 \times T_a^4} \quad (2)$$

in which ε is the emissivity, assumed to be 0.99 (typical value for dense vegetation). T_{bg} is the background temperature (K).

$\triangle T$ (°C) and *CWSI* were calculated as Equations (3) and (4):

$$\Delta T = T_s - T_a \quad (3)$$

$$CWSI = \frac{T_s - T_{pot}}{T_{dry} - T_{pot}} \quad (4)$$

The parameters T_{pot} (°C) and T_{dry} (°C) denote the surface canopy temperature of a winter wheat plant when transpiration is at its maximum rate (T_{pot}) and when the plant is not transpiring at all (T_{dry}). T_{pot} and T_{dry} were computed directly for each measurement day utilizing the histogram method in this study. They were determined as the surface temperatures corresponding to the 1st percentile (T_{pot}) and 99th percentile (T_{dry}) of the polygon records observed on flying day.

2.4. Field Sampled Data Acquisition and Determination

A SPAD Chlorophyll Meter (SPAD-502Plus, Minolta, Osaka, Japan) measured the SPAD values of the first fully expanded leaf, with the average calculated from three random measurements per leaf. Each plot's average SPAD value was determined from ten leaves. Therefore, 15 sets of data in each growth stage were obtained, resulting in a total of 90 sets of data obtained in 2021 and 75 sets of data obtained in 2022.

Simultaneously, destructive sampling was conducted to identify the plant N status. Two rows of 30 cm long segments (avoiding boundary rows) were sampled. The above-ground biomass (*AGB*) for each plot was measured after oven-drying samples at 105 °C for 1 h, then at 75 °C until constant weight. Plant nitrogen concentration (*PNC*) was analyzed using the Kjeldahl method, and plant N accumulation (*PNA*) values were calculated for each plot [57] (Equation (5)):

$$PNA_a = PNC_a \times AGB \quad (5)$$

where PNA_a is the plant's actual measured N accumulation (g m^{-2}), PNC_a is the plant's actual measured N concentration (%), and *AGB* is the above-ground biomass (g m^{-2}).

The critical plant N concentration (PNC_c, %) is required for optimal AGB production, and is calculated using the critical N dilution curve (Equation (6)) developed by Yue et al. [58], from data collected in sixteen nitrogen rate experiments in the North China Plain between 2000 and 2011:

$$PNC_c = 4.15 \times (AGB/100)^{-0.38} \quad (6)$$

The N nutrition index (*NNI*) is defined as the ratio of PNA_a to PNA_c * AGB (Equation (7)):

$$NNI = PNA_a/(PNC_c \times AGB) \quad (7)$$

In each plot, winter wheat was harvested from a 1 m^2 area at maturity and threshed to determine grain yield (at 13% moisture content). Relative yield (*RY*) was calculated

as the ratio of grain yield at a specific N rate to the highest yield recorded across all N application rates.

2.5. Statistical Analysis and Machine Learning Algorithm

To effectively reduce data dimensionality and integrate information from multiple sensors [59,60], principal component analysis (PCA) was employed to reduce the number of independent variables while preserving as much relevant information as possible [61]. For CIs and VIs, the top 10 indices with the highest correlation coefficients with SPAD, PNA, and NNI were selected. Principal components (PCs) were retained based on eigenvalues exceeding one, following the Kaiser criterion. The cumulative variance explained by the retained PCs was calculated to ensure that more than 95% of the total variance was preserved. The original feature space was transformed into a new space defined by the selected PCs. Each PC was interpreted based on the loading values, identifying the contribution of individual indices.

The ensemble learning algorithm called XGBoost (extreme gradient boosting) was used to evaluate winter wheat N status. Based on a boosting strategy [62], XGBoost improves a weak learner, specifically the CART model, by analyzing learning errors and adjusting sample weights iteratively [63]. The objective function is defined as Equation (8):

$$obj = \sum_{i=1}^{m} L(y_i, \hat{y}_i) + \sum_{k=1}^{n} \Omega(f_k) \quad (8)$$

The model's accuracy is closely tied to its hyperparameters. In this study, a grid search method was used to explore the optimal combination of hyperparameters, including: learning rate [0.01, 0.05, 0.1], max tree depth [3, 5, 7], *n* estimators [100, 200, 500], min child weight [1, 5, 10], and reg alpha [0, 0.1, 0.5, 1]. These hyperparameters were optimized through tenfold cross-validation and grid search on training datasets. Other parameters were set as follows: gamma = 0.1, max delta step = 0, subsample = 0.5 and colsample bytree = 0.7. Data analyses were conducted using Jupyter Notebook with Python 3.10.

Figure 4 illustrates the flowchart of this study, outlining data acquisition and processing, feature extraction and analysis from multiple images, and the development and comparison of models. The dataset obtained from the two-year winter wheat experiment was joined for analysis. To discern the specific attributes of wheat during different growth stages, the mixed dataset was divided into two sub-datasets based on the pre-heading stage (combining tillering, jointing, and booting) and the post-heading stage (combining heading, flowering, and filling). Ensuring the robustness and comprehensiveness of the models with designated input variables, we used the 2021 dataset to train the data, and the 2022 dataset as an independent test dataset. First, the top 10 indices of correlation between RGB and multispectral sensors with SPAD, PNA, and NNI, as well as the two temperature indices, were used for PCA. Then, the selection of the top *n* principal components (PCs) from one sensor (CIs or VIs) or multiple sensors (CIs + TIs, CIs + Vis, and CIs + TIs + VIs) followed the criterion of eigenvalues exceeding one. These selected PCs were employed as input variables for the XGBoost model. Subsequently, the PCs for 2022 were derived through spectral information and the eigenvectors from data of 2021. The dependent variables were SPAD, PNA, and NNI.

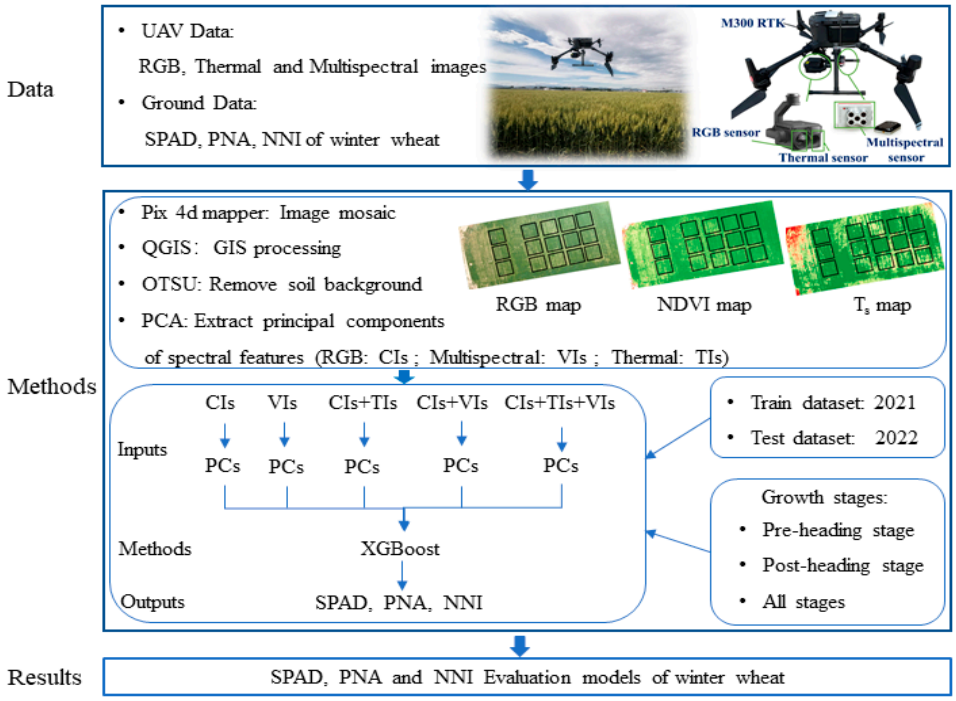


Figure 4. The general workflow of the study. CIs, color indices; TIs, thermal indices; VIs, vegetation indices; PCs, principal components; PNA, plant nitrogen accumulation; NNI, nitrogen nutrient index; XGBoost, extreme gradient boosting algorithm.

One-way analysis of variance analysis (ANOVA) was used to test whether the different N fertilizer application rates had a significant effect on SPAD, PNA, and NNI at the 0.05 probability level. Curves and figures were drawn with Origin 2023 Pro software (Origin Lab Corporation One Roundhouse Plaza, Northampton, MA, USA). The model's performance was assessed using the coefficient of determination (Equation (9)), root mean square error (Equation (10)), and normalized root mean square error (Equation (11)):

$$R^2 = 1 - \frac{\sum_{i=1}^{n}(y_i - \hat{y}_i)^2}{\sum_{i=1}^{n}(y_i - \overline{y_i})^2} \quad (9)$$

$$\mathrm{RMSE} = \sqrt{\frac{1}{n}\left(\sum_{i=1}^{n}(y_i - \hat{y}_i)^2\right.} \quad (10)$$

$$\mathrm{NRMSE} = \frac{\sqrt{\frac{1}{n}\sum_{i=1}^{n}(y_i - \hat{y}_i)^2}}{\bar{y}} \times 100\% \quad (11)$$

where y_i is the measured value of SPAD, PNA, or NNI, $\hat{y}_i$ is the predicted value of SPAD, PNA, and NNI, the average of the measured values is represented by $\overline{y}$, and n refers to the total number of samples.

3. Results

3.1. Statistical Characteristics of Winter Wheat Nitrogen Indicators

3.1.1. SPAD and Plant Nitrogen Accumulation

SPAD and PNA showed significant differences between the different treatments (Figures 5 and 6) ($p < 0.05$). Notably, SPAD and PNA had higher values with increasing N application, with the highest values from the N4 treatment and the lowest from the N0 treatment. Across both years of the experiment, the N0, N1, and N2 treatments

exhibited differences among themselves and from all other treatment levels in relation to SPAD and PNA. The N3 and N4 treatments presented relatively similar values, with the N4 treatment consistently displaying slightly higher values, but not differing significantly from the N3 treatment in most growth stages. Overall, the N application experiments provided a well-suited dataset marked by substantial variability, thereby facilitating the objectives of this study.

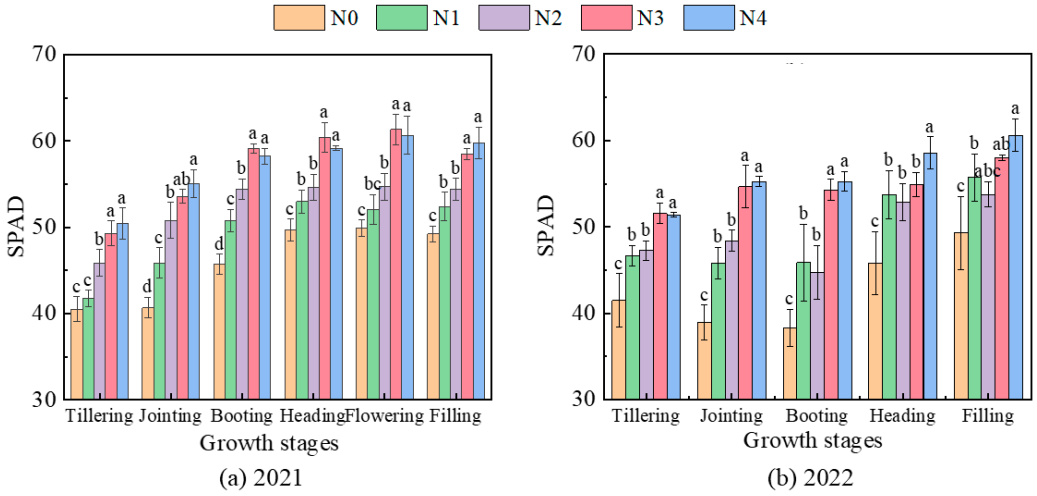


Figure 5. SPAD of winter wheat in the experiment. Note: Means followed by different letters among N treatments differ significantly at $p < 0.05$.

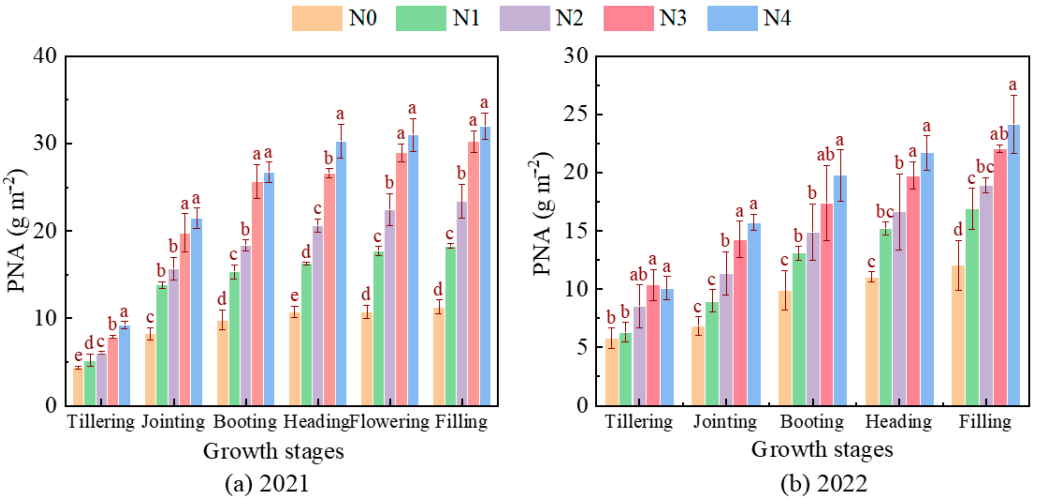


Figure 6. The plant N accumulation of winter wheat in the experiment. Note: Means followed by different letters among N treatments differ significantly at $p < 0.05$.

3.1.2. Nitrogen Nutrition Index

The critical N concentration curve established in prior studies and the measured AGB and PNC and are shown in Figure 7 to validate the reliability of NNI in this experiment. Following analysis of variance, the data obtained from different N treatments were divided into a N-limiting group (N0, N1, N2, and N3 treatments) and a non-N-limiting group (N4 treatment). PNC of winter wheat in the N-limiting group at different growth stages in 2021 was distributed below the curve, while that of non-N-limiting group was generally distributed above the curve. In the subsequent year, deviations were observed at tillering and jointing stages. This discrepancy arose from the combination of higher PNC and lower AGB of winter wheat. Consequently, certain data points from the N-limiting group surpassed

the critical N concentration curve, resulting in diminished verification efficacy. However, the verification accuracy improved at winter wheat booting, heading, and filling stages.

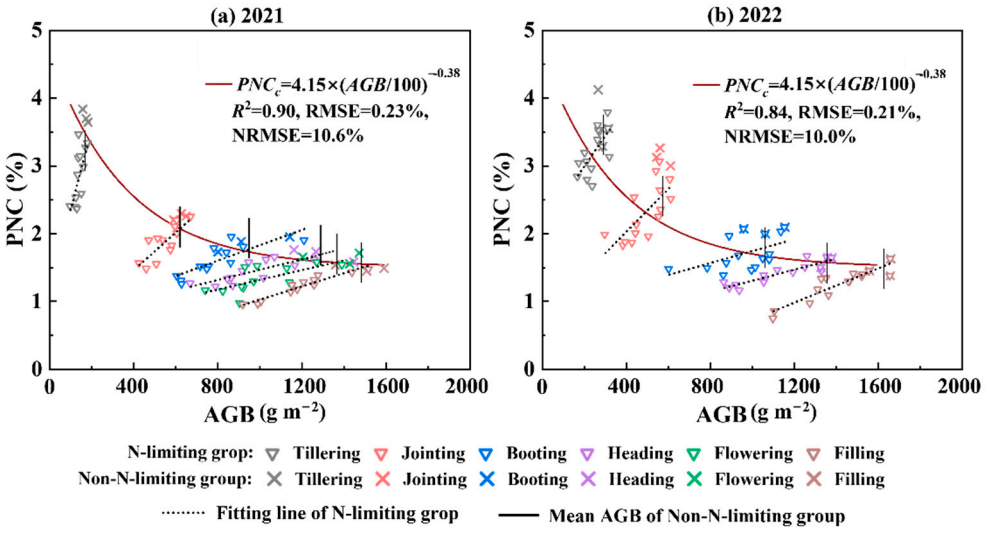


Figure 7. The critical nitrogen dilution curve of winter wheat.

Based on the critical N concentration curve, NNI was calculated using the AGB and PNA data obtained in this experiment. The significance analysis results for NNI under different treatments are shown in Figure 8. It is evident that N treatment effects on wheat growth varied across different growth stages and years. Significant NNI levels were observed during the heading stage in 2021 and early growth stages in 2022 for certain treatments, highlighting the effectiveness of N application during these periods. Conversely, the N0 treatment consistently showed insufficient nitrogen supply across all stages.

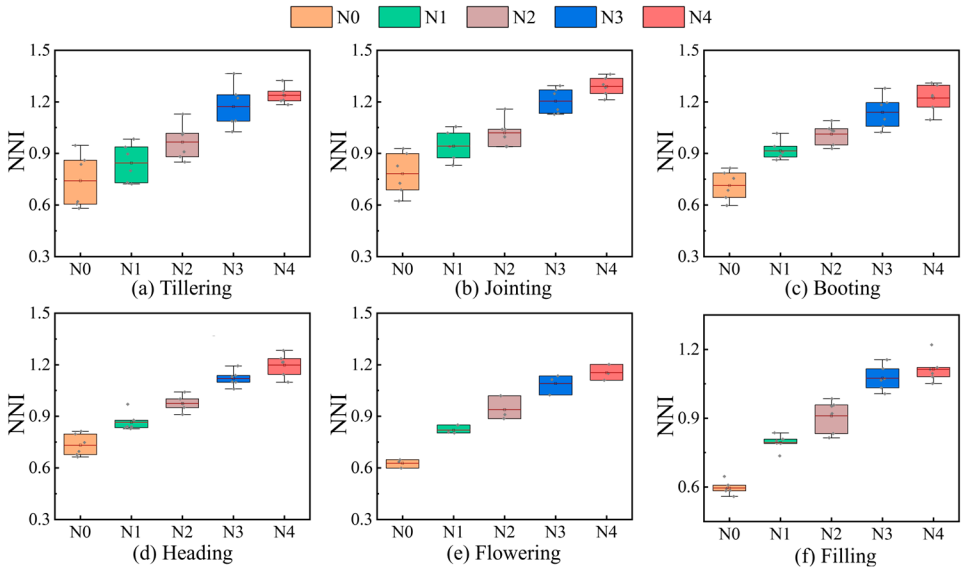


Figure 8. The N nutrition index of winter wheat in the experiment.

Figure 9 shows the correlation between winter wheat RY and NNI. It can be seen that NNI and RY were consistent with the changing trend of linear regression plus platform. The turning point of NNI was 1.14, 1.24, 1.16, 1.15, 1.11, and 1.09 at tillering, jointing, booting, heading, flowering, and filling stages, respectively. Similarly, the relationship between RY and NNI adhered to a downward-opening quadratic function. In general, the N treatment experiment in this study can better match the critical N concentration curve established

by previous studies, so the calculated NNI can reflect the nitrogen deficit status of wheat. Overall, the N treatment experiments fitted well with the critical N concentration curve, so the calculated NNI effectively reflects the N deficit status of winter wheat, facilitating a more precise assessment of nutritional requirements.

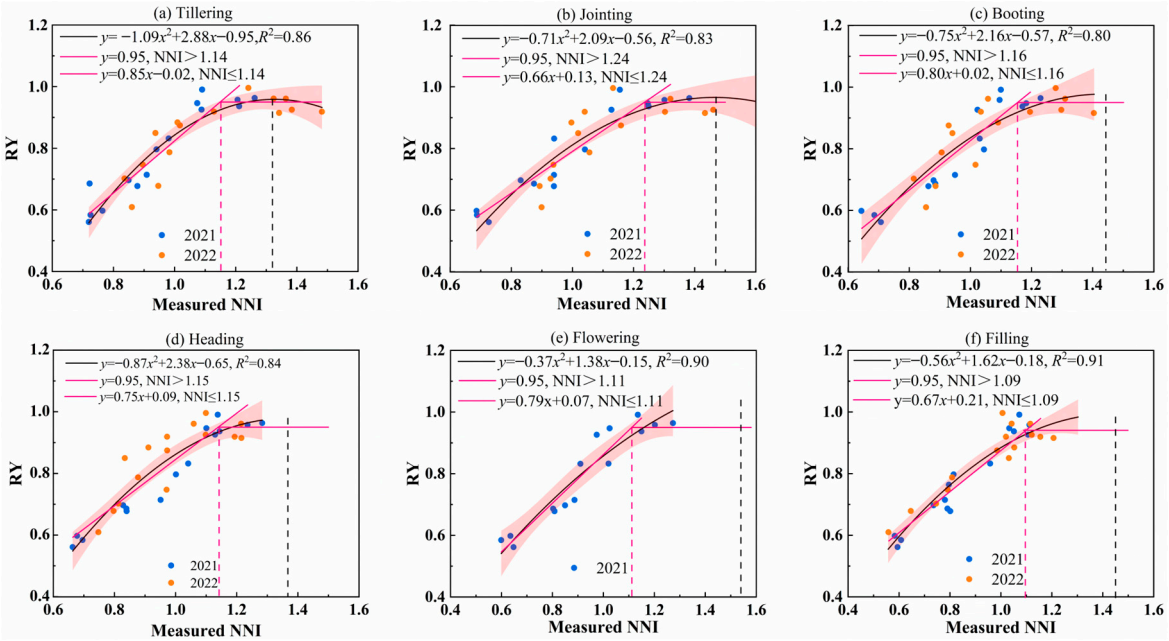


Figure 9. Relationship between winter wheat RY and NNI. RY and NNI represent relative yield and nitrogen nutrition index, respectively. The gray zones represent the 95% confidence interval of the fitted quadratic function.

3.2. Relationship Between Wheat Nitrogen Indicators and Remote Sensing Variables

The Pearson coefficients (r) between wheat N indicators and CIs, VIs, and TIs were calculated across the growth stages (Figures 10–12). At the pre-heading stage, high correlations were found between SPAD values and CIs, such as *NDLuv* (r = 0.70 in 2021 and r = 0.67 in 2022) and *red* (r = −0.65 in 2021 and r = −0.67 in 2022) (Figure 10a). *RGRI* and *H* performed best in the post-heading stage, followed closely by *NDLab* and *ExR*. For the overall data, the CIs with the highest correlations with SPAD were *ExGR* (r = 0.67) and red (r = −0.65). The top five CIs most correlated with SPAD were *red*, *ExR*, *ExGR*, *H*, and *NDLuv* across all stages when data from 2021 and 2022 were combined. For the VIs (Figure 10b), *NDRE*, *NDVI*, and *GNDVI* showed high correlations with SPAD at the pre-heading stage. The correlation between most VIs and SPAD improved in the post-heading stage, and the |r| values of *NDVI*, *NDRE*, *GNDVI*, and *TCARI* reached above 0.61 in the 2-year data. *NDRE* was most correlated with SPAD in all stages (r = 0.67 in 2021 and r = 0.65 in 2022). When 2-year data were combined, *NDVI*, *NDRE*, *GNDVI*, *TCARI*, and *RERVI* had the highest correlations with SPAD in all stages. Overall, the performance of the best-performing VIs and CIs was very similar. Correlations between SPAD and the TIs (Figure 10c) were considerably lower. The r values of TIs with SPAD ranged from −0.22 to −0.50, −0.27 to −0.64, and −0.32 to −0.50 in the pre-heading, post-heading, and all stages, respectively.

Figure 11 shows the correlations between PNA and CIs (Figure 11a), VIs (Figure 11b), and TIs (Figure 11c). Most CIs showed higher correlation with PNA in the pre-heading stage than in the post-heading stage. *ExG* (r = 0.65), *ExGR* (r = 0.67), *ExR* (r = −0.67), *MGRVI* (r = 0.68), and *H* (r = 0.66) correlated best with PNA when combining the data of 2021 and 2022 in the pre-heading, post-heading, and all stages, respectively. Except for *EVI*, *DVI*, and *MCARI*, most VIs showed high correlations (|r| > 0.45) with PNA. *RVI*, *NDRE*, *GNDVI*,

and *SIPI* were constantly well correlated with PNA across the growth stages, with r values ranging from 0.55 to 0.75, 0.61 to 0.77, 0.50 to 0.67, and −0.51 to −0.67, respectively.

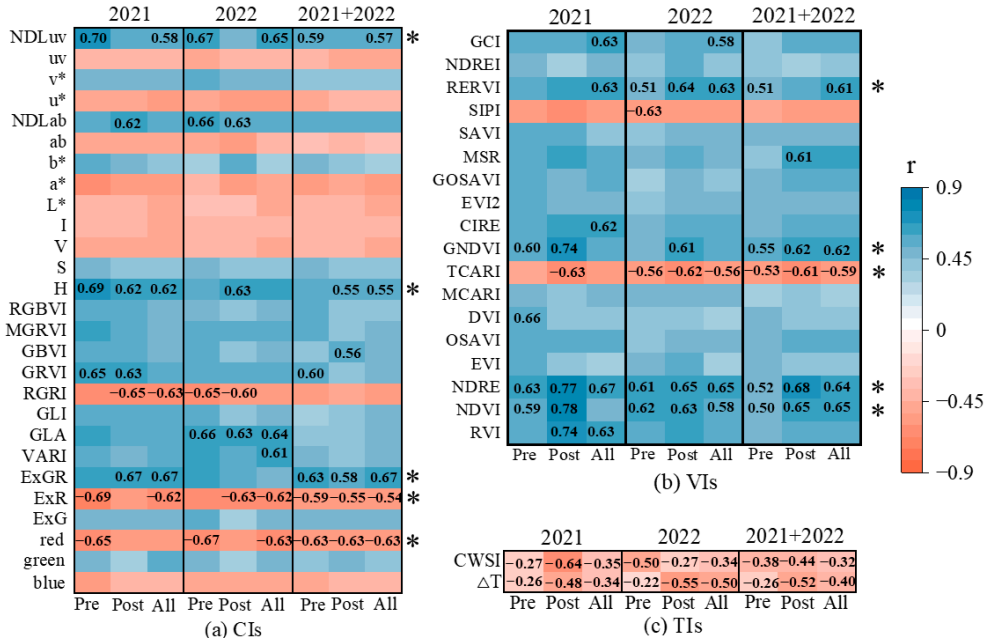


Figure 10. Correlation between CIs, VIs, TIs, and SPAD of winter wheat. CIs, VIs, and TIs stand for color indices, vegetation indices, and temperature indices. Asterisks (*) indicate the indices that were within the top 5 of the best performing CIs and VIs by combining 2021 and 2022 in all stages.

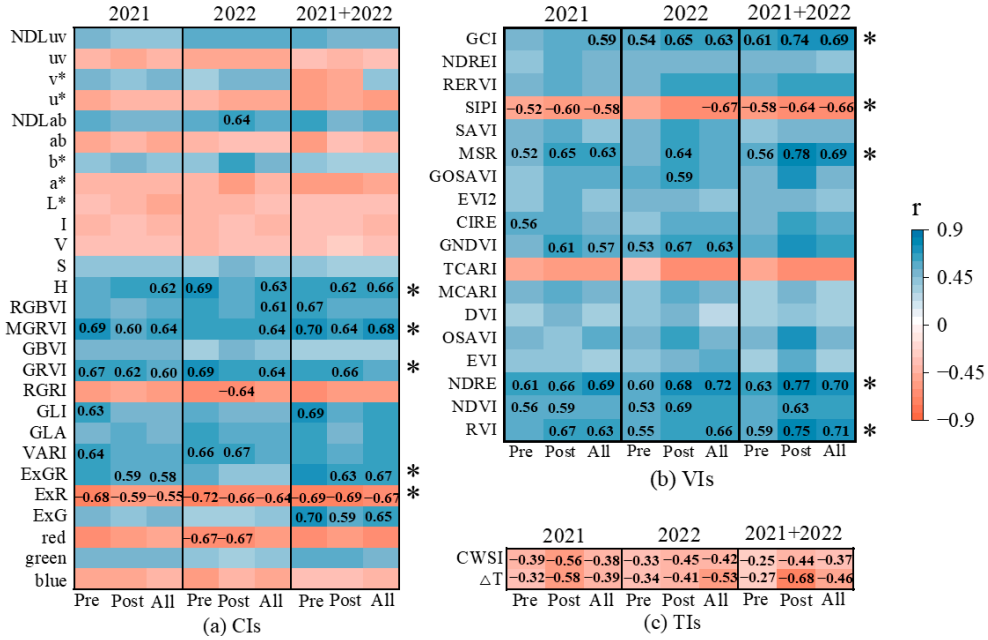


Figure 11. Correlation between CIs, VIs, TIs, and PNA of winter wheat. PNA represents plant nitrogen accumulation. CIs, VIs, and TIs stand for color indices, vegetation indices, and temperature indices. Asterisks (*) indicate the indices that were within the top 5 best performing CIs and VIs by combining 2021 and 2022 in all stages.

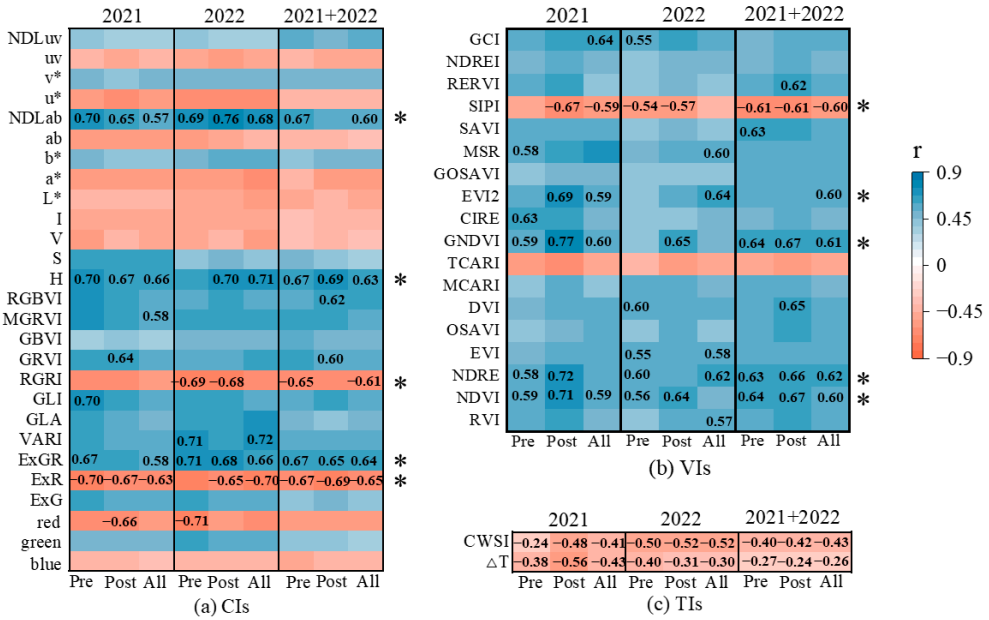


Figure 12. Correlation between CIs, VIs, TIs, and NNI of winter wheat. NNI represents the nitrogen nutrient index. CIs, VIs, and TIs stand for color indices, vegetation indices, and temperature indices. Asterisks (*) indicate the indices that were within the top 5 of the best performing CIs and VIs by combining 2021 and 2022 in all stages.

The correlations between TIs and PNA in the post-heading stage (r values ranging from −0.41 to −0.68) were higher than those in the pre-heading stage (r values ranging from −0.25 to −0.39). The two-year data were well correlated, which provided a stable dataset for this study.

For the CIs, *ExR*, *ExGR*, *RGRI*, *H*, and *NDLab* showed high correlations with NNI when all data are combined (Figure 12). Similar to the PNA, the VIs had a stronger correlation with NNI in the post-heading stage than in the pre-heading stage. Among these VIs, *NDVI* and *GNDVI* produced the highest correlation with NNI in the pre-heading stage (r = 0.64 by combining 2021 and 2022), while *NDVI* and *NDRE* produced the highest correlation (r = 0.67 by combining 2021 and 2022) in the post-heading stage. Except for *DVI* and *CIRE*, the absolute values of r between VIs and NNI reached above 0.50 in all stages when pooling the data from 2021 and 2022. In total, spectral responses varied across growth stages, influenced by the dynamic nature of crop nitrogen uptake and canopy development. In early stages, high-resolution RGB indices were more effective for nitrogen estimation due to soil background noise. As the canopy matured, red-edge indices and thermal data became more reliable, reflecting their sensitivity to physiological and structural changes.

3.3. Principal Component Analysis of Spectral Index

A comprehensive array of the top 10 CIs and VIs with higher correlation with SPAD, PNA, and NNI was employed in the PCA for calculating the top PCs. The first two principal components are shown in Figure 13 for analyses of CIs, VIs, and combinations of CIs + TIs, CIs + VIs, and CIs + TIs + VIs by combining the data of 2021 and 2022. For the PCA of the CIs (Figure 13a), 95.0% of the data variation was explained by the first two components. The *VARI*, *GRVI*, *MGRVI*, and *H* were strongly positively, and *a**, *ExR*, and *RGRI* were strongly negatively correlated to PC1, with *NDLuv* more correlated with PC2 (Figure 13a). For the PCA of VIs (Figure 13b), the first principal component explained 77.8% of the variance, while the second principal component explained 12.9% of the variance. The top two PCs explained 83.2% and 83.1% of the variation in the CIs + TIs and CIs + VIs,

respectively. For the CIs + TIs (Figure 13c), nearly all CIs were very strongly correlated with PC1, and the two TIs as well as *NDLuv* were positively correlated with PC2. For the CIs + VIs (Figure 13d), *NDLab*, *TCARI*, and green leaf index *GLI* were most strongly correlated with PC1. These were also the variables relating most strongly to PC1 for the combination of CIs + TIs + VIs (Figure 13e), where both TIs correlated more with PC2.

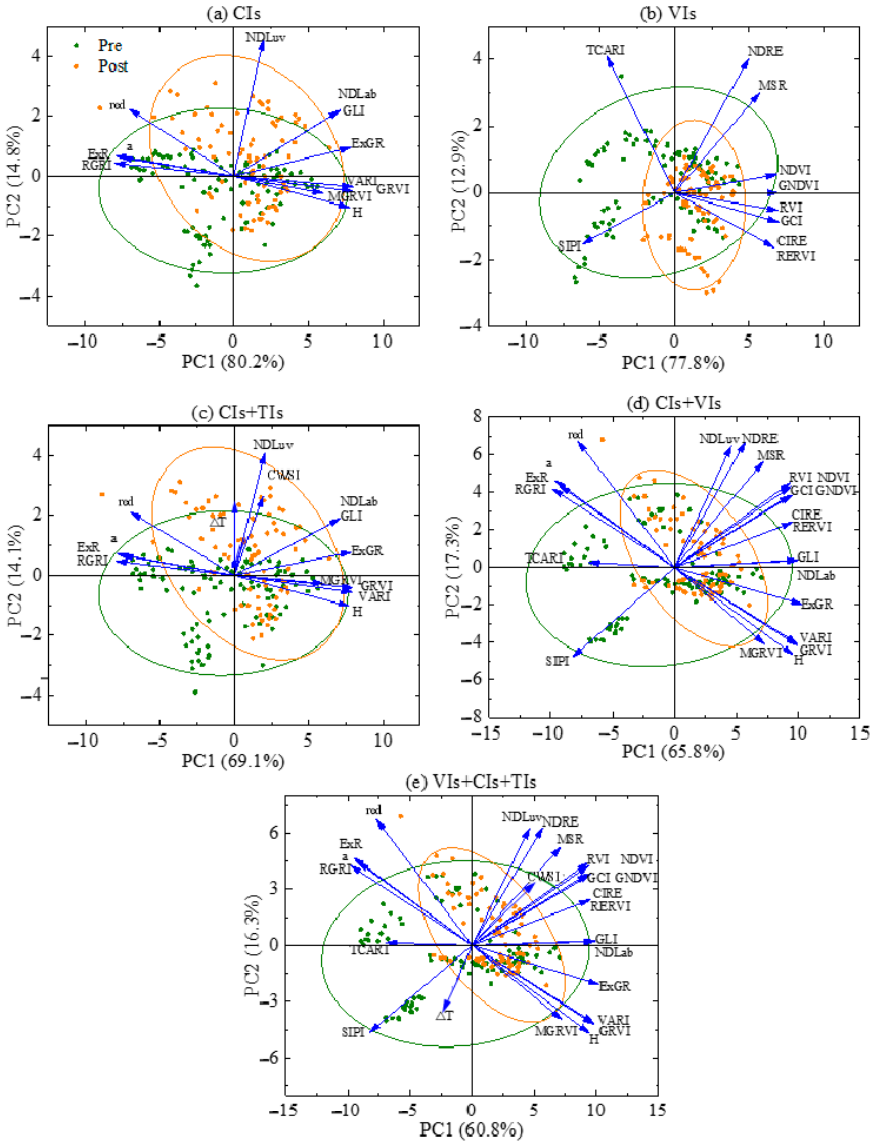


Figure 13. Principal component axes 1 and 2 of the PCA performed on the color indices (CIs), vegetation indices (VIs), and thermal indices (TIs) by combining 2021 and 2022.

Table 5 shows the number of principal components (PCs) used as inputs for the XGBoost model (eigenvalue > 1 was retained). The cumulative contribution variance reached more than 95% for all models.

Table 5. The number of PCs and cumulative contribution variance of PCA as input for the models.

PCA Results	CIs	VIs	CIs + TIs	CIs + VIs	CIs + TIs + VIs
PCs	4	4	5	6	6
Contribution variance (%)	98.1	96.0	96.8	97.0	95.2

Note: CIs, TIs, and VIs represent color indices, thermal indices, and vegetation indices, respectively. PCs represents principal components.

3.4. Estimation Nitrogen Models of Winter Wheat Using Different Sensors

The XGBoost models for SPAD, PNA, and NNI estimation were validated using the independent test dataset of 2022 (Table 6). The results of the train dataset can be seen in Table A3 (Appendix A). There was little difference in the model accuracy of the SPAD model based on CIs at the pre-heading stage and the post-heading stage. Model accuracy dropped when data from all growth stages were mixed, especially for NNI (R^2 = 0.64 (pre-heading stage), R^2 = 0.65 (post-heading stage) and R^2 = 0.53 (all stages)). The SPAD models based on VIs achieved better test results at the post-heading stage (R^2 = 0.70, RMSE = 4.89, NRMSE = 8.8%) compared to the pre-heading stage (R^2 = 0.61, RMSE = 5.01, NRMSE = 10.1%). Similar results were obtained for PNA and NNI. CIs outperformed VIs in all SPAD, PNA, and NNI estimation models in the pre-heading stage. However, the models built using VIs achieved higher accuracy in the post-heading stage and all stages compared to CIs. Models based on CIs explained 66%, 68%, and 64% of the variability at the pre-heading stage, and 67%, 67%, and 65% in the post-heading stage, of SPAD, PNA, and NNI, respectively. For the models based on VIs, the results in the post-heading stage improved compared with the pre-heading stage, with R^2 increasing from 0.61 to 0.70 (SPAD), from 0.64 to 0.73 (PNA), and from 0.60 to 0.67 (NNI), respectively. SPAD and NNI models built by CIs and VIs using separate datasets of pre-heading and post-heading stages obtained better test results than the combined datasets of both stages. The test results of PNA in different stages varied.

Table 6. Model test results of nitrogen estimation models of winter wheat.

		SPAD			PNA (g m^{-2})			NNI		
		R^2	RMSE	NRMSE (%)	R^2	RMSE	NRMSE (%)	R^2	RMSE	NRMSE (%)
Pre	CIs	0.66	4.53	9.1%	0.68	3.61	23.5%	0.64	0.16	14.5%
	VIs	0.61	5.01	10.1%	0.64	3.87	25.1%	0.60	0.18	16.1%
	CIs + TIs	0.69	4.32	8.7%	0.70	3.43	22.3%	0.65	0.16	14.1%
	CIs + VIs	0.74	3.32	6.7%	0.78	3.10	20.1%	0.68	0.15	13.2%
	CIs + VIs + TIs	0.75	3.29	6.6%	0.81	3.04	19.8%	0.71	0.15	12.9%
Post	CIs	0.67	5.02	9.0%	0.67	5.77	22.6%	0.65	0.15	14.4%
	VIs	0.70	4.89	8.8%	0.73	5.24	20.5%	0.67	0.14	13.5%
	CIs + TIs	0.74	4.33	7.8%	0.77	4.61	18.0%	0.70	0.12	11.7%
	CIs + VIs	0.77	4.06	7.3%	0.77	4.62	18.1%	0.72	0.12	11.6%
	CIs + VIs + TIs	0.79	3.88	6.9%	0.81	4.43	17.3%	0.73	0.11	11.2%
All	CIs	0.56	5.95	11.3%	0.64	5.78	28.7%	0.53	0.23	22.1%
	VIs	0.60	5.63	10.7%	0.68	4.93	24.5%	0.57	0.21	20.5%
	CIs + TIs	0.65	4.99	9.5%	0.71	4.78	23.7%	0.61	0.19	17.8%
	CIs + VIs	0.71	4.42	8.4%	0.80	3.65	18.1%	0.66	0.18	16.9%
	CIs + VIs + TIs	0.71	4.31	8.2%	0.79	3.79	18.8%	0.64	0.18	17.2%

Note: PNA and NNI represent plant nitrogen accumulation and nitrogen nutrient index, respectively. CIs, TIs, and VIs represent color indices, thermal indices, and vegetation indices, respectively.

Models built with both CIs and VIs markedly improved the model performance compared to their respective single-sensor models. Adding TIs to the CIs also improved the models' performance throughout, but the models were not as good as the CIs + VIs-based models. Finally, the models combining information from the three sensors (CIs + VIs + TIs) obtained the best results in all models at the pre-heading stage and post-heading stage for all three variables, and when all stages were combined for SPAD models. CI + VI-based model performance exceeded that of CI + VI + TI-based models for PNA and NNI when both growth stages were considered, although the differences between them were small.

As can be observed in Figure 14, the predicted values of the five schemes were in good linear correlation with the measured values of SPAD, PNA, and NNI. The results indicated that the XGBoost algorithm significantly ($p < 0.01$) predicted winter wheat SPAD, PNA, and NNI under different N treatments. However, it can also be seen that the models typically overestimated at low values and underestimated at high values, especially in the pre-heading stage and all stages of SPAD and NNI.

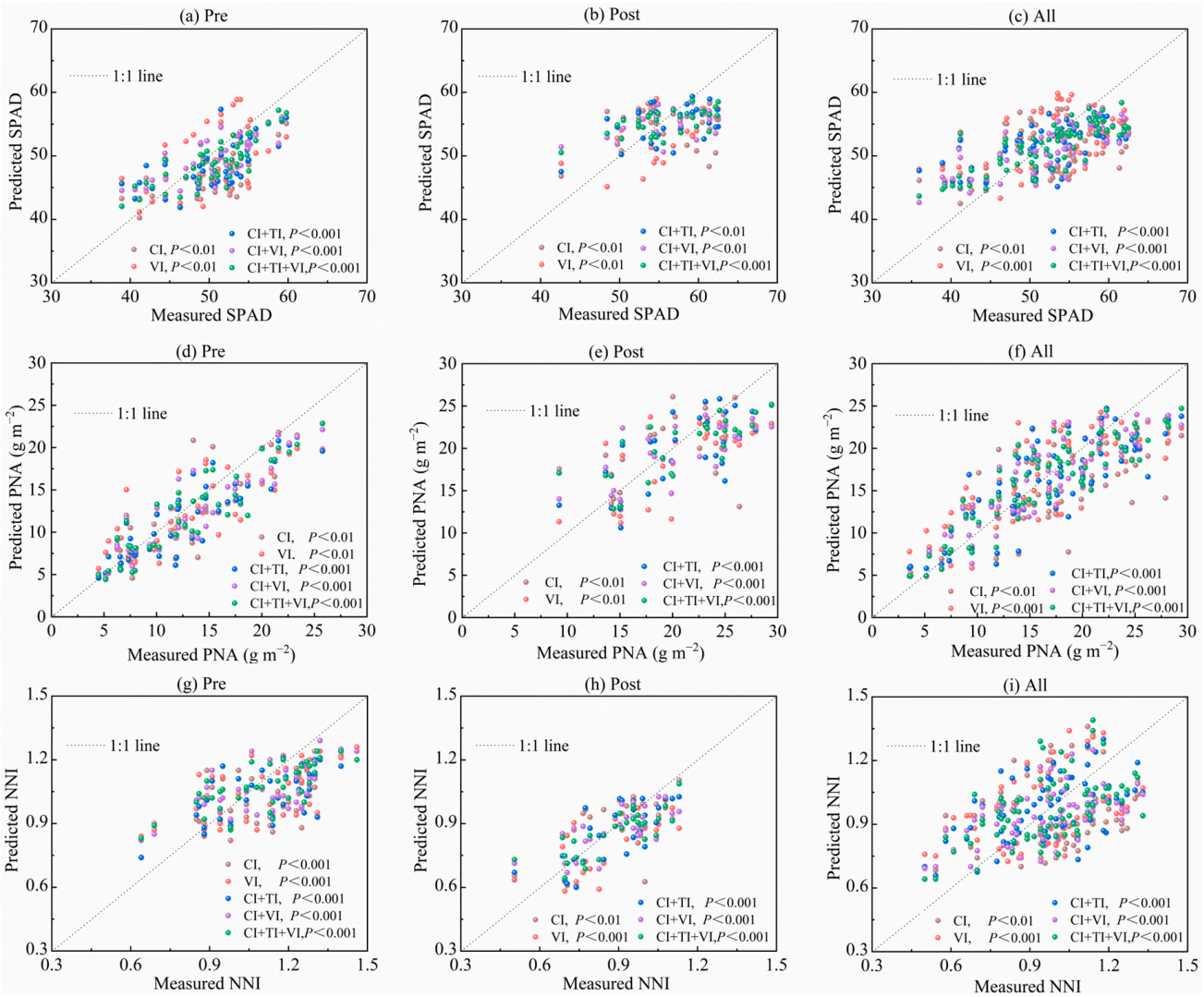
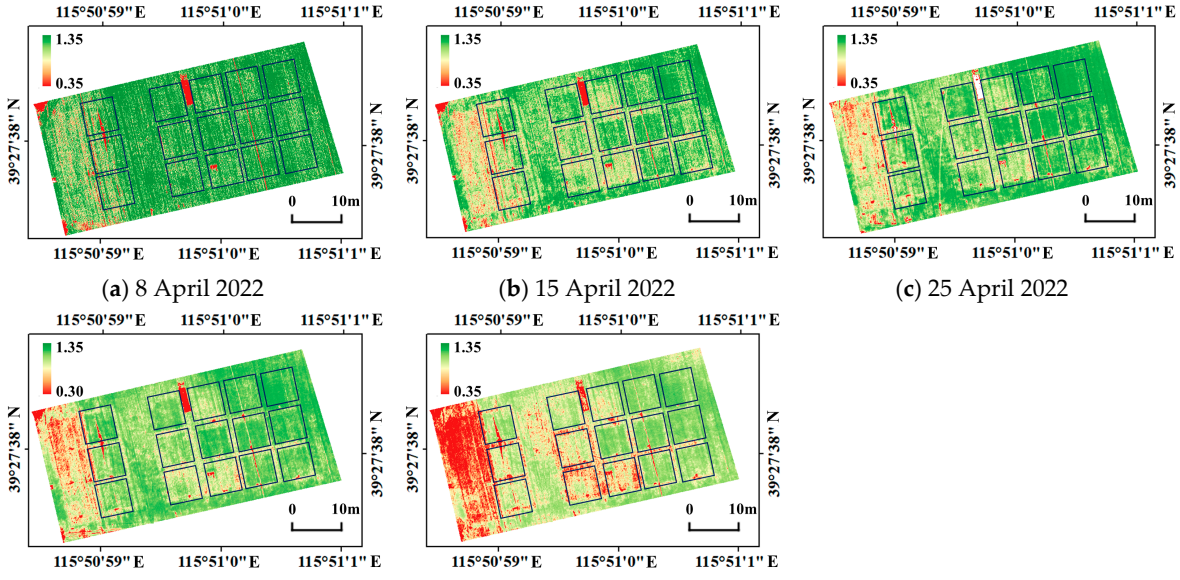


Figure 14. Relationships between the predicted and measured values. SPAD (**a**–**c**). PNA (**d**–**f**). NNI (**g**–**i**). PNA and NNI represent plant nitrogen accumulation and nitrogen nutrient index, respectively. CI, TI, and VI represent color index, thermal index, and vegetation index, respectively.

The model for predicting all growth stages of NNI using the XGBoost algorithm by combining data from RGB, multispectral, and thermal sensors is shown in Figure 15. The N fertilizer stress on winter wheat varies at different growth stages. It is consistent with the differences in NNI thresholds at different growth stages in Figure 9.



(**a**) 8 April 2022 (**b**) 15 April 2022 (**c**) 25 April 2022

(**d**) 4 May 2022 (**e**) 14 May 2022

Figure 15. The NNI map of winter wheat based on the all-stage estimation model using CIs, VIs, and TIs. NNI represents nitrogen nutrient index. CIs, VIs, and TIs represent color indices, vegetation indices, and thermal indices, respectively.

4. Discussion

4.1. Assessement of Wheat Nitrogen Using UAV-Based Sensors: Monitoring Nitrogen Dilution and Growth Stage Variability

Remote sensing data derived from UAV multispectral, RGB, and thermal sensors provide valuable information about plant N content and distribution. The concept of plant nitrogen dilution, typically observed during rapid growth phases, can be monitored through changes in the spectral reflectance characteristics, especially in the red-edge and near-infrared regions, which are closely linked to chlorophyll content and plant physiological processes. As plants enter reproductive stages, the distribution of dry matter and N transport often leads to a decrease in N concentration, which can be detected through remote sensing techniques [10,63]. In this study, the results from 2021 (R^2 = 0.90, NRMSE = 10.6%) and 2022 (R^2 = 0.84, NRMSE = 10.0%) confirmed the regional applicability of the PNC_c curve for diagnosing winter wheat N status and demonstrated the stability of N concentration and AGB across growth seasons [64,65]. By incorporating nitrogen dilution curves, we identified spectral indices that account for both chlorophyll content and biomass accumulation, providing a mechanistic basis for feature selection. Furthermore, the use of PCA revealed that the dominant spectral indices shifted from RGB-derived indices in early stages to red-edge and thermal indices in later stages, aligning with changes in nitrogen demand and canopy structure. Furthermore, NNI thresholds varied at different growth stages (Figure 9); however, NNI below thresholds does not necessarily indicate N deficiency, as factors such as drought stress [66] and the interaction of phosphorus and potassium [67,68] can also influence soil N availability and the plants' N translocation.

The observed tendency of the models to overestimate or underestimate N indicators can be attributed to stage-specific and sensor-related factors (Figure 14). During early growth stages, sparse vegetation increases the influence of soil background reflectance, leading to overestimated nitrogen levels. Conversely, in late growth stages, dense canopy conditions often result in the saturation of spectral indices, causing underestimation of nitrogen levels. To address these biases, several strategies are recommended. Firstly, soil-adjusted indices and high-resolution RGB data can be utilized to minimize soil interfer-

ence during early growth stages, particularly in sparsely vegetated conditions. Secondly, nonlinear regression methods and ensemble models offer promising solutions to handle saturation effects in dense canopies, enhancing the accuracy of nitrogen predictions. Finally, the integration of additional environmental variables, such as soil and weather data, can provide complementary information to improve model robustness.

4.2. Performance of the UAV Multiple Sensors in Estimating Wheat N Status During Different Growth Stages

The CI, VI, and TI data were extracted from RGB, multispectral, and thermal images captured using a UAV platform. During the pre-heading stage, CI-based models outperformed VI-based models in diagnosing winter wheat N status, likely due to their heightened sensitivity to color changes indicating early-stage crop nitrogen deficiencies [69,70]. For instance, CIs such as ExG and ExGR achieved higher correlations with SPAD and PNA compared to VIs. Meanwhile, the higher resolution of RGB images may make a greater contribution to removing soil noise than multispectral images when estimating winter wheat N status [16]. However, the accuracy of CI-based models tends to decrease noticeably at the post-heading stage, reflecting their greater sensitivity to crop growth parameters before canopy closure [32]. At post-heading stage, as crop canopies close and biomass accumulates, VIs derived from multispectral sensors become more effective. Jiang et al. (2020) noted similar findings in their UAV multispectral monitoring of winter wheat NNI, achieving higher model accuracy in late growth stages (R^2 = 0.71–0.81) compared to early growth stages (R^2 = 0.48–0.52) [57]. This divergence can be attributed to sparse vegetation during early growth stages, where spectral reflectance is notably influenced by bare soil surfaces [71]. The phenotypic observations collected from multispectral imaging display a hysteresis, detecting variations in crop canopy structure more effectively during later growth stages. This pattern is consistent with prior studies encompassing leaf area index and leaf dry matter [72]. In addition, thermal data demonstrated its greatest contribution during the late growth. Compared to using only CIs, the enhancement derived from combining CIs and TIs was more pronounced during the post-heading stage, indicating that this characteristic was more likely to be observed at the later stages of crop growth [12]. The contribution of thermal data is more pronounced during the post-heading stage when nitrogen demand is high, and physiological responses to N stress are more noticeable.

It is evident that SPAD estimation models (NRMSE = 6.6%–11.3%) performed better than PNA (NRMSE = 17.3%–28.7%) and NNI (NRMSE = 11.2%–22.1%). This is likely because SPAD measurements are based on remote sensing (absorption and transmittance in the red and near-infrared spectra), which align closely with UAV-based data. Conversely, PNA and NNI reflect overall N leaf levels, with only about 1.7% and 19% of total N allocated to chlorophyll and the light-harvesting complex, respectively [69].

The synergy of UAV multi-sensors has been instrumental in improving crop growth status estimation results. We found that the combination of CIs and VIs markedly enhanced model performance compared to models utilizing either CIs or VIs across all growth stages. CIs capture fine-scale color variations, which are most indicative of early-stage N deficiencies. VIs provide insights into chlorophyll content and biomass accumulation, which are crucial during later growth stages. TIs detect temperature variations, which reflect N status beyond optical measurements. By combining these indices, the models leverage high-resolution spatial data (RGB), robust spectral information (multispectral), and physiological metrics (thermal), resulting in improved N prediction accuracy across all growth stages.

4.3. Contribution of Thermal Data to Nitrogen Diagnosis of Winter Wheat

In our study, most models demonstrated optimal outcomes when TIs were incorporated into CI + VI configurations, although the net effect was relatively limited. Pei et al. found that different N application rates had a significant impact on wheat canopy temperature [73]. This was also observed in a recent study involving winter wheat N content models that integrated RGB, multispectral, and thermal features [20]. Thermal sensors offer complementary information by capturing canopy temperature, which is closely linked to plant physiological responses to N application [74]. This contribution is distinct from CIs and VIs, which primarily focus on chlorophyll content and biomass. The observed benefits can be attributed to three key factors. Firstly, increased N application enhances photosynthesis and stomatal conductance, leading to higher transpiration rates, which cool the plant canopy. Thermal sensors capture this cooling effect and detect changes in water stress and transpiration, providing an indirect yet sensitive indicator of plant health and N status [14,75]. Secondly, insufficient N application results in reduced growth, poor tillering, and increased susceptibility to water stress, which collectively raise canopy temperatures. Thermal sensors can directly capture these stress indicators, offering information not reflected in optical data [13,76]. Lastly, thermal data enhance the overall diagnostic capability of models by adding a layer of information on water stress and physiological conditions, which is absent in CIs and VIs. PCA (Figure 13) shows that thermal information is distinct and not fully represented by CIs or VIs, indicating that thermal sensors play a unique and complementary role in N status assessment compared to RGB and multispectral sensors.

4.4. Evaluation and Limitations of Winter Wheat Nitrogen Estimation Models

Despite the fact that we have used an independent test dataset, the performance of the machine learning model compares relatively favorably to other studies. Jiang et al. [57] using a fixed-wing drone, achieved R^2 values of 0.82–0.87 and RMSE of 0.11–0.12 for NNI, and R^2 values of 0.83–0.84 and RMSE of 1.3–1.7 g m^{-2} for PNA. However, their model incorporated multispectral remote sensing, meteorological parameters, and field management variables, thereby introducing experimental complexity. Liu et al. [77] identified an index 'G–B' based on UAV RGB images as a robust vegetation index for SPAD prediction (RMSE = 2.71, NRMSE = 6.5%), but their study lacked a truly independent test set. Although existing studies indicate challenges in developing generalized models adaptable to various growth stages due to differing optimal predictors across stages, this study adopted a holistic approach that encompassed diverse growth stages. By defining pre-heading and post-heading stages based on winter wheat's vegetative and reproductive growth phases in this study, it was not necessary to use stage-specific models in subsequent tests. Remarkably, the models produced commendable performance across different growth stages, indicating the potential of the ensemble method for evaluating winter wheat N nitrogen status using UAV remote sensing in future growing seasons.

Nonetheless, this study presents some limitations. This study refrained from conducting an exhaustive comparison of accuracy across various machine learning algorithms, although previous research supports XGBoost's superior performance in monitoring crop growth [78,79] and predicting yields [80]. This is attributed to its fusion of decision trees and optimized hyperparameter selection [63]. The diverse N-fertilization treatments applied to winter wheat were designed to simulate real-world scenarios, resulting in varying N nutrition statuses and providing a broad dataset for model training and testing. One limitation of this study is the possible biases introduced by the specific years (2021 and 2022) and field conditions in which the experiments were conducted. The weather patterns, soil characteristics, and other environmental factors across these years may have influenced the results, particularly the stability of winter wheat PNC and AGB. This may limit the gen-

eralizability of the findings to other years or conditions, as crop responses to N fertilization can vary significantly with different climatic and soil conditions. Another consideration is the scalability of this approach to different crops or geographic locations. While the UAV remote sensing technology and the PNC_c curve proved effective for winter wheat in the studied region, the applicability of this method to other crops or regions with different environmental conditions remains uncertain. For instance, crops with varying growth habits, N use efficiency, or canopy structures may require adjustments to the monitoring protocols or the development of crop-specific PNC_c curves. Furthermore, the practical application of this approach at a larger scale presents additional challenges. Although UAVs offer a flexible and relatively accessible means of monitoring crop N status, the integration of more complex instrumentation, such as hyperspectral sensors or LiDAR, could enhance model accuracy. However, these technologies may introduce cost and operational complexities, potentially limiting their widespread adoption in large-scale farming. The potential of using alternative devices, such as satellite-based sensors or ground-based platforms, could also be explored to overcome these limitations, offering different alternatives between resolution, cost, and ease of deployment. This study did not engage in N application decision-making. To attain comprehensive validation, it is imperative to extend the scope of investigation by incorporating data spanning multiple years or diverse geographical areas in subsequent research.

5. Conclusions

This study demonstrates the effectiveness of UAV-based remote sensing in monitoring the N status of winter wheat across different growth stages using multi-sensor models. The results indicated that CIs of ExGR, H, and NDLab showed stronger correlations with SPAD, PNA, and NNI in the early growth stages. Conversely, VIs of GNDVI, NDRE, and NDVI, alongside two temperature indices ($\triangle$T and CWSI), demonstrated superior performance in the late growth stages. Model performance varied significantly across growth stages, with CI-based models exceling during pre-heading, while VI-based models were superior during post-heading and overall. The addition of TIs to CIs notably enhanced model accuracy post-heading compared to CIs alone, with R^2 increasing from 0.67 to 0.74 (SPAD), from 0.67 to 0.77 (PNA), and from 0.65 to 0.70 (NNI). Furthermore, the combination of CIs and VIs consistently improved predictive accuracy across pre-heading, post-heading, and all stages. It is noteworthy that models encompassing the combined data from all three sensors consistently exhibited the highest levels of accuracy, except for PNA and NNI at all stages, where CI + VI-based models delivered superior performance. This study provides a dependable framework for leveraging UAV-based remote sensing techniques to improve data fusion and model performance, contributing to advancements in precision monitoring and modeling of crop conditions.

Author Contributions: Formal analysis, J.W., S.L., X.H. and H.Z.; Funding acquisition, H.Y.; Investigation, J.W., W.W. and S.L.; Methodology, J.W. and X.H.; Software, W.W.; Supervision, H.Y. and W.H.M.; Validation, W.H.M.; Visualization, H.Z.; Writing—original draft, J.W.; Writing—review and editing, H.Y. and W.H.M. All authors have read and agreed to the published version of the manuscript.

Funding: This research was funded by Key Research and Development Program of Hebei Province (Grant No. 21327002D), Water Conservancy Technology Demonstration Project of China (Grant No. SF–202311), Key Research and Development Program of Shandong Province of China (Grant No. 2022CXGC020707), National Key Research and Development Program of China (Grant No. 2023YFD1900704) and China Agriculture Research System (Grant No. CARS–03).

Data Availability Statement: The authors confirm that the data supporting the findings of this study are available within the article.

Conflicts of Interest: The authors declare no conflicts of interest.

Appendix A

Table A1. Overview of the color indices (CIs—indices derived from RGB data) used in this study.

CIs	Name	Formula
red	Normalized R	$red = R/(R+G+B)$
green	Normalized G	$green = G/(R+G+B)$
blue	Normalized B	$blue = B/(R+G+B)$
ExG	Excess green index	$ExG = 2\times g-r-b$
ExR	Excess red index	$ExR = 1.4\times r-g$
ExGR	Excess green minus excess red index	$ExGR = 3\times g-2.4\times r-b$
VARI	Visible atmospherically resistance index	$VARI = (g-r)/(g+r-b)$
GLA	Green leaf algorithm	$GLA = (2\times g-r+b)/(2\times g+r+b)$
GLI	Green leaf index	$GLI = (2\times g-r-b)/(2\times g+r+b)$
RGRI	Red green ratio index	$RGRI = r/g$
GRVI	Green–red vegetation index	$GRVI = (g-r)/(g+r)$
NDYI	Normalized difference yellowness index	$NDYI = (g-b)/(g+b)$
MGRVI	Modified green–red vegetation index	$MGRVI = (g^2-r^2)/(g^2+r^2)$
RGBVI	Red–green–blue vegetation index	$RGBVI = (g^2-b\times r)/(g^2+b\times r)$
H	Hue	$H = 60^\circ\times(g-b)/(C_{max}-C_{min})$ if $C_{max}= r$; $H = 60^\circ\times(b-r)/(C_{max}-C_{min})+120$ if $C_{max}= g$; $H = 60^\circ\times(r-g)/(C_{max}-C_{min})+240$ if $C_{max}= b$; $(C_{max}= max(r,g,b), C_{min}= min(r,g,b))$
S	Saturation	$S = (C_{max}-C_{min})/C_{max}$
V	Value	$V = C_{max}$
I	Intensity	$I = (C_{max}+C_{min})/2$
*L**	Lightness	$L^*= 116\,(Y/Y^0)^{1/3}-16$ if $Y/Y^0> 0.008856$; $L^*= 903.3(Y/Y^0)$ otherwise $\left(Y = 0.213r+0.751g+0.072b,\ Y^0= 100\right)$
*a**	Green–Red component	$a^*= 500\times\left[(X/X^0)^{1/3}-(Y/Y^0)^{1/3}\right]$ $(X = 0.421r+0.358g+0.180b, X^0= 95.047)$
*b**	Blue–Yellow component	$b^*= 200\times\left[(Y/Y^0)^{1/3}-(Z/Z^0)^{1/3}\right]$ $(Z = 0.019r+0.119g+0.950b,\ Z^0= 108.883)$
ab	–	$ab = a^*\times b^*$
NDLab	Normalized difference CIELab index	$NDLab = (1-a^*-b^*)/(1-a^*+b^*)+1$
*u**	Green–Red component	$u^*= 13L[4X/(X+15Y+3Z)]-4X^0/(X^0+15Y^0+3Z^0)$
*v**	Blue–Yellow component	$v^*= 13L[9X/(X+15Y+3Z)]-9Y^0/(X^0+15Y^0+3Z^0)$
uv	–	$uv = u^*\times v^*$
NDLuv	Normalized difference CIELuv index	$NDLuv = (1-u^*-v^*)/(1-u^*+v^*)+1$

Note: R, G, and B represent the average digital number values for each plot obtained from the RGB images, with values ranging from 0 to 255.

Table A2. Overview of the vegetation indices (VIs—indices derived from multispectral data) used in this study.

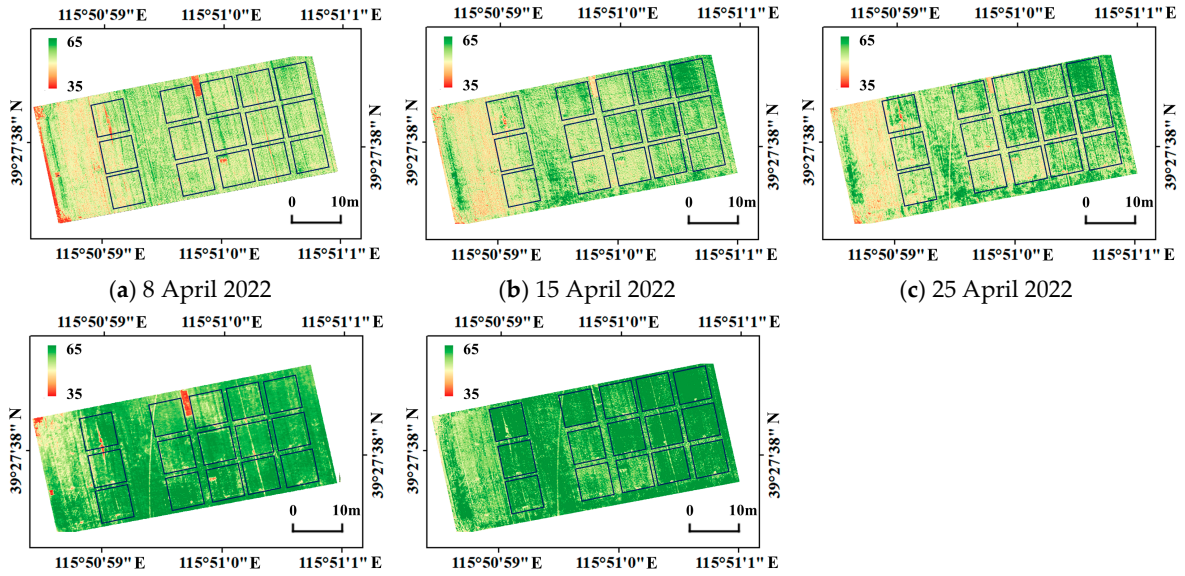
VIs	Name	Formula
RVI	Ratio vegetation index	$RVI = NIR/R$
NDVI	Normalized difference vegetation index	$NDVI = (NIR - R)/(NIR + R)$
NDRE	Normalized difference red-edge index	$NDRE = (NIR - RE)/(NIR + RE)$
EVI	Enhanced vegetation index	$EVI = 2.5 \times (NIR - R)/(NIR + 6R - 7.5B + 1)$
OSAVI	Optimized soil adjusted vegetation index	$OSAVI = 1.16 \times (NIR - R)/(NIR + R + 0.16)$
DVI	Difference vegetation index	$DVI = NIR - R$
MCARI	Modified chlorophyll absorption in reflectance index	$MCARI = [(RE - R) - 0.2 \times (RE - G)] \times (RE/R)$
TCARI	Transformed chlorophyll absorption in reflectance index	$TCARI = 3 \times [(RE - R) - 0.2 \times (RE - G) \times (RE/R)]$
GNDVI	Green normalized difference vegetation index	$GNDVI = (NIR - G)/(NIR + G)$
CIRE	Red-edge chlorophyll index	$CIRE = NIR/RE - 1$
EVI2	Enhanced vegetation index	$EVI2 = 2.5 \times (NIR - R)/(NIR + 2.4R + 1)$
GOSAVI	Green optimal soil adjusted vegetation index	$GOSAVI = 1.16 \times (NIR - G)/(NIR + G + 0.16)$
MSR	Modified simple ratio index	$MSR = (NIR/R - 1)/(NIR/R + 1)^{0.5}$
SAVI	Soil adjusted vegetation index	$SAVI = 1.5 \times (NIR - R)/(NIR + R + 0.5)$
SIPI	Structure insensitive pigment index	$SIPI = (NIR - B)/(NIR - R)$
RERVI	Red-edge vegetation index	$RERVI = NIR/RE$
NDREI	Normalized difference red-edge index	$NDREI = (RE - G)/(RE + G)$
GCI	Green chlorophyll index	$GCI = NIR/G - 1$

Note: R, G, B, NIR, and RE represent the reflectance values of wheat in the red, green, blue, near-infrared, and red-edge bands, captured by the multispectral camera.

Table A3. Model training results of nitrogen indicator models in different growth stages.

Growth Stages		SPAD			PNA (g m^{-2})			NNI		
		R^2	RMSE	NRMSE (%)	R^2	RMSE	NRMSE (%)	R^2	RMSE	NRMSE (%)
Pre	CIs	0.69	4.01	8.5	0.71	2.34	18.0	0.69	0.14	14.0
	VIs	0.68	4.15	8.8	0.68	2.51	19.3	0.72	0.13	13.0
	CIs + TIs	0.74	3.44	7.3	0.75	1.99	15.3	0.76	0.11	11.1
	CIs + VIs	0.78	3.07	6.5	0.76	1.92	14.7	0.80	0.10	9.7
	CIs + TIs + VIs	0.78	3.01	6.4	0.77	1.82	14.0	0.82	0.09	9.1
Post	CIs	0.74	4.03	7.4	0.76	3.01	13.5	0.67	0.15	16.0
	VIs	0.77	3.66	6.7	0.81	2.53	11.3	0.72	0.13	13.4
	CIs + TIs	0.79	3.41	6.3	0.81	2.25	10.1	0.75	0.11	11.7
	CIs + VIs	0.80	3.23	5.9	0.86	1.95	8.7	0.76	0.10	11.1
	CIs + TIs + VIs	0.81	3.04	5.6	0.86	1.89	8.5	0.80	0.09	9.6
All	CIs	0.66	4.63	9.1	0.71	3.35	19.6	0.63	0.17	17.0
	VIs	0.71	4.14	8.1	0.73	3.21	18.8	0.69	0.16	15.7
	CIs + TIs	0.81	3.52	6.9	0.8	2.66	15.6	0.73	0.13	13.2
	CIs + VIs	0.84	3.09	6.1	0.82	2.34	13.7	0.75	0.12	12.2
	CIs + VIs + TIs	0.84	3.12	6.1	0.83	2.21	12.9	0.75	0.13	12.5

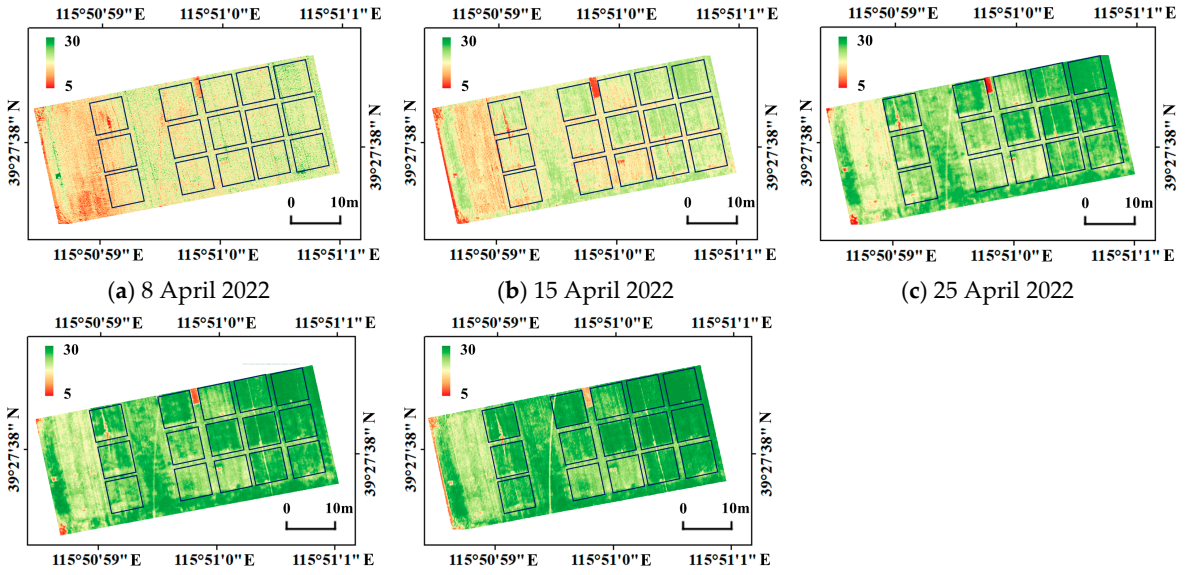
Note: PNA and NNI represent plant nitrogen accumulation and nitrogen nutrient index, respectively. Pre, post, and all represent pre-heading stage, post-heading stage, and all growth stages, respectively. CIs, TIs, and VIs represent color indices, thermal indices, and vegetation indices, respectively.



(**a**) 8 April 2022 (**b**) 15 April 2022 (**c**) 25 April 2022

(**d**) 4 May 2022 (**e**) 14 May 2022

Figure A1. The SPAD map of winter wheat based on the all-stage estimation model using CIs, VIs, and TIs.



(**a**) 8 April 2022 (**b**) 15 April 2022 (**c**) 25 April 2022

(**d**) 4 May 2022 (**e**) 14 May 2022

Figure A2. The PNA (g m^{-2}) map of winter wheat based on the all-stage estimation model using CIs, VIs, and TIs.

References

1. Evans, J.R.; Clarke, V.C. The Nitrogen Cost of Photosynthesis. *J. Exp. Bot.* **2019**, *70*, 7–15. [CrossRef] [PubMed]
2. Cai, D.; Shoukat, M.R.; Zheng, Y.; Tan, H.; Sun, M.; Yan, H. Improving Wheat Grain Yield and Nitrogen Use Efficiency by Optimizing the Fertigation Frequency Using Center Pivot Irrigation System. *Water* **2023**, *15*, 1932. [CrossRef]
3. Berger, K.; Verrelst, J.; Féret, J.B.; Wang, Z.; Wocher, M.; Strathmann, M.; Danner, M.; Mauser, W.; Hank, T. Crop Nitrogen Monitoring: Recent Progress and Principal Developments in the Context of Imaging Spectroscopy Missions. *Remote Sens. Environ.* **2020**, *242*, 111758. [CrossRef] [PubMed]
4. Kong, L.; Xie, Y.; Hu, L.; Si, J.; Wang, Z. Excessive Nitrogen Application Dampens Antioxidant Capacity and Grain Filling in Wheat as Revealed by Metabolic and Physiological Analyses. *Sci. Rep.* **2017**, *7*, srep43363. [CrossRef]
5. Zhang, M.; Wang, H.; Yi, Y.; Ding, J.; Zhu, M.; Li, C.; Guo, W.; Feng, C.; Zhu, X. Effect of Nitrogen Levels and Nitrogen Ratios on Lodging Resistance and Yield Potential of Winter Wheat (*Triticum aestivum* L.). *PLoS ONE* **2017**, *12*, e0187543. [CrossRef]

6. Tripathi, S.C.; Sayre, K.D.; Kaul, J.N.; Narang, R.S. Growth and Morphology of Spring Wheat (*Triticum aestivum* L.) Culms and Their Association with Lodging: Effects of Genotypes, N Levels and Ethephon. *Field Crops Res.* **2003**, *84*, 271–290. [CrossRef]
7. Lichtfouse, E.; Navarrete, M.; Debaeke, P.; Souchère, V.; Alberola, C. *Sustainable Agriculture*; Springer: Dordrecht, The Netherlands, 2009; ISBN 9789048126651. [CrossRef]
8. Zhang, F.; Cui, Z.; Chen, X.; Ju, X.; Shen, J.; Chen, Q.; Liu, X.; Zhang, W.; Mi, G.; Fan, M.; et al. Integrated Nutrient Management for Food Security and Environmental Quality in China. *Adv. Agron.* **2012**, *116*, 1–40. [CrossRef]
9. Inoue, Y. Satellite- and Drone-Based Remote Sensing of Crops and Soils for Smart Farming—A Review. *Soil Sci. Plant Nutr.* **2020**, *66*, 798–810. [CrossRef]
10. Feng, D.; Xu, W.; He, Z.; Zhao, W.; Yang, M. Advances in Plant Nutrition Diagnosis Based on Remote Sensing and Computer Application. *Neural Comput. Appl.* **2020**, *32*, 16833–16842. [CrossRef]
11. Feng, L.; Chen, S.; Zhang, C.; Zhang, Y.; He, Y. A Comprehensive Review on Recent Applications of Unmanned Aerial Vehicle Remote Sensing with Various Sensors for High-Throughput Plant Phenotyping. *Comput. Electron. Agric.* **2021**, *182*, 106033. [CrossRef]
12. Mon, J.; Bronson, K.F.; Hunsaker, D.J.; Thorp, K.R.; White, J.W.; French, A.N. Interactive Effects of Nitrogen Fertilization and Irrigation on Grain Yield, Canopy Temperature, and Nitrogen Use Efficiency in Overhead Sprinkler-Irrigated Durum Wheat. *Field Crops Res.* **2016**, *191*, 54–65. [CrossRef]
13. Lo, T.H.; Rudnick, D.R.; DeJonge, K.C.; Bai, G.; Nakabuye, H.N.; Katimbo, A.; Ge, Y.; Franz, T.E.; Qiao, X.; Heeren, D.M. Differences in Soil Water Changes and Canopy Temperature Under Varying Water × Nitrogen Sufficiency for Maize. *Irrig. Sci.* **2020**, *38*, 519–534. [CrossRef]
14. Coast, O.; Harden, S.; Conaty, W.C.; Brodrick, R.; Edwards, E.J. Canopy Temperature of High-Nitrogen Water-Stressed Cotton. *Crop Sci.* **2020**, *60*, 1513–1529. [CrossRef]
15. Scholarsarchive, B.; Carroll, D.A. Drought and Nitrogen Effects on Maize Canopy Temperature and Stress Indices. Master's Thesis, Brigham Young University, Provo, UT, USA, 2015. Available online: https://scholarsarchive.byu.edu/etd/5932 (accessed on 18 July 2024).
16. Xu, X.; Fan, L.; Li, Z.; Meng, Y.; Feng, H.; Yang, H.; Xu, B. Estimating leaf nitrogen content in corn based on information fusion of multiple-sensor imagery from UAV. *Remote Sens.* **2021**, *13*, 340. [CrossRef]
17. Xu, S.; Xu, X.; Blacker, C.; Gaulton, R.; Zhu, Q.; Yang, M.; Yang, G.; Zhang, J.; Yang, Y.; Yang, M.; et al. Estimation of Leaf Nitrogen Content in Rice Using Vegetation Indices and Feature Variable Optimization with Information Fusion of Multiple-Sensor Images from UAV. *Remote Sens.* **2023**, *15*, 854. [CrossRef]
18. Wang, J.; Lou, Y.; Wang, W.; Liu, S.; Zhang, H.; Hui, X.; Wang, Y.; Yan, H.; Maes, W.H. A Robust Model for Diagnosing Water Stress of Winter Wheat by Combining UAV Multispectral and Thermal Remote Sensing. *Agric. Water Manag.* **2024**, *291*, 108616. [CrossRef]
19. Bertalan, L.; Holb, I.; Pataki, A.; Négyesi, G.; Szabó, G.; Kupásné Szalóki, A.; Szabó, S. UAV-Based Multispectral and Thermal Cameras to Predict Soil Water Content—A Machine Learning Approach. *Comput. Electron. Agric.* **2022**, *200*, 107262. [CrossRef]
20. Ding, F.; Li, C.; Zhai, W.; Fei, S.; Cheng, Q.; Chen, Z. Estimation of Nitrogen Content in Winter Wheat Based on Multi-Source Data Fusion and Machine Learning. *Agriculture* **2022**, *12*, 1752. [CrossRef]
21. Matese, A.; Di Gennaro, S.F. Practical Applications of a Multisensor UAV Platform Based on Multispectral, Thermal and RGB High Resolution Images in Precision Viticulture. *Agriculture* **2018**, *8*, 116. [CrossRef]
22. Liu, Q.; Wang, C.; Jiang, J.; Wu, J.; Wang, X.; Cao, Q.; Tian, Y.; Zhu, Y.; Cao, W.; Liu, X. Multi-Source Data Fusion Improved the Potential of Proximal Fluorescence Sensors in Predicting Nitrogen Nutrition Status Across Winter Wheat Growth Stages. *Comput. Electron. Agric.* **2024**, *219*, 108786. [CrossRef]
23. Shirazi, M.A.; Boersma, L. A Unifying Quantitative Analysis of Soil Texture. *Soil Sci. Soc. Am. J.* **1984**, *48*, 142–147. [CrossRef]
24. Daniels, L.; Eeckhout, E.; Wieme, J.; Dejaegher, Y.; Audenaert, K.; Maes, W.H. Identifying the Optimal Radiometric Calibration Method for UAV-Based Multispectral Imaging. *Remote Sens.* **2023**, *15*, 2909. [CrossRef]
25. Noburuki, O. A Threshold Selection Method from Gray-Level Histograms. *IEEE Trans. Syst. Man Cybern.* **1979**, *9*, 62–66. [CrossRef]
26. Meyer, G.E.; Neto, J.C. Verification of Color Vegetation Indices for Automated Crop Imaging Applications. *Comput. Electron. Agric.* **2008**, *63*, 282–293. [CrossRef]
27. Woebbecke, D.M.; Meyer, G.E.; Von Bargen, K.; Mortensen, D.A. Color Indices for Weed Identification Under Various Soil, Residue, and Lighting Conditions. *Am. Soc. Agric. Biol. Eng.* **1995**, *38*, 259–269. [CrossRef]
28. Yang, B.; Wang, M.; Sha, Z.; Wang, B.; Chen, J.; Yao, X.; Cheng, T.; Cao, W.; Zhu, Y. Evaluation of Aboveground Nitrogen Content of Winter Wheat Using Digital Imagery of Unmanned Aerial Vehicles. *Sensors* **2019**, *19*, 4416. [CrossRef]

29. Saberioon, M.M.; Gholizadeh, A. Novel Approach for Estimating Nitrogen Content in Paddy Fields Using Low Altitude Remote Sensing System. In Proceedings of the International Archives of the Photogrammetry, Remote Sensing and Spatial Information Sciences—ISPRS Archives, Prague, Czech Republic, 12–19 July 2016; International Society for Photogrammetry and Remote Sensing: Hannover, Germany, 2016; pp. 1011–1015. [CrossRef]
30. Louhaichi, M.; Borman, M.M.; Johnson, D.E. Spatially Located Platform and Aerial Photography for Documentation of Grazing Impacts on Wheat. *Geocarto Int.* **2001**, *16*, 65–70. [CrossRef]
31. Verrelst, J.; Schaepman, M.E.; Koetz, B.; Kneubühler, M. Angular Sensitivity Analysis of Vegetation Indices Derived from CHRIS/PROBA Data. *Remote Sens. Environ.* **2008**, *112*, 2341–2353. [CrossRef]
32. Hunt, E.R., Jr.; Cavigelli, M.; Daughtry, C.S.T.; Mcmurtrey Iii, J.; Walthall, C.L. Evaluation of Digital Photography from Model Aircraft for Remote Sensing of Crop Biomass and Nitrogen Status. *Precis. Agric.* **2005**, *6*, 359–378. [CrossRef]
33. Sulik, J.J.; Long, D.S. Spectral Considerations for Modeling Yield of Canola. *Remote Sens. Environ.* **2016**, *184*, 161–174. [CrossRef]
34. Bendig, J.; Yu, K.; Aasen, H.; Bolten, A.; Bennertz, S.; Broscheit, J.; Gnyp, M.L.; Bareth, G. Combining UAV-Based Plant Height from Crop Surface Models, Visible, and near Infrared Vegetation Indices for Biomass Monitoring in Barley. *Int. J. Appl. Earth Obs. Geoinf.* **2015**, *39*, 79–87. [CrossRef]
35. Possoch, M.; Bieker, S.; Hoffmeister, D.; Bolten, A.A.; Schellberg, J.; Bareth, G. Multi-Temporal Crop Surface Models Combined with the Rgb Vegetation Index from UAV-Based Images for Forage Monitoring in Grassland. In Proceedings of the International Archives of the Photogrammetry, Remote Sensing and Spatial Information Sciences—ISPRS Archives, Prague, Czech Republic, 12–19 July 2016; International Society for Photogrammetry and Remote Sensing: Hannover, Germany, 2016; pp. 991–998. [CrossRef]
36. Cheng, H.D.; Jiang, X.H.; Sun, Y.; Wang, J. Color Image Segmentation: Advances and Prospects. *Pattern Recognit.* **2001**, *34*, 2259–2281. [CrossRef]
37. Buchaillot, M.L.; Gracia-Romero, A.; Vergara-Diaz, O.; Zaman-Allah, M.A.; Tarekegne, A.; Cairns, J.E.; Prasanna, B.M.; Araus, J.L.; Kefauver, S.C. Evaluating Maize Genotype Performance Under Low Nitrogen Conditions Using RGB UAV Phenotyping Techniques. *Sensors* **2019**, *19*, 1815. [CrossRef] [PubMed]
38. Jordan, C.F.; Jordan1, C.F.; Rico, P.; Center, N.; Piedras, R. Derivation of leaf-area index from quality of light on the forest floor. *Ecology* **1969**, *50*, 660–663. Available online: https://www.jstor.org/stable/1936256 (accessed on 20 November 2024). [CrossRef]
39. Rouse, R.W.H.; Haas, J.A.W.; Deering, D.W. Monitoring Vegetation Systems in the Great Plains with ERTS. NASA. In Proceedings of the Goddard Space Flight Center 3d ERTS-1 Symposium, Washington, DC, USA, 10–14 December 1973; 1974; Volume 1.
40. Fitzgerald, G.; Rodriguez, D.; O'Leary, G. Measuring and Predicting Canopy Nitrogen Nutrition in Wheat Using a Spectral Index—The Canopy Chlorophyll Content Index (CCCI). *Field Crops Res.* **2010**, *116*, 318–324. [CrossRef]
41. Liu, H.Q.; Huete, A. A Feedback Based Modification of the NDVI to Minimize Canopy Background and Atmospheric Noise. *IEEE Trans. Geosci. Remote Sens.* **2019**, *33*, 457–465. [CrossRef]
42. Rondeaux, G.; Steven, M.; Baret, F. Optimization of Soil-Adjusted Vegetation Indices. *Remote Sens. Environ.* **1996**, *55*, 95–107. [CrossRef]
43. Broge, N.H.; Mortensen, J. Deriving Green Crop Area Index and Canopy Chlorophyll Density of Winter Wheat from Spectral Reflectance Data. *Remote Sens. Environ.* **2002**, *81*, 45–57. [CrossRef]
44. Daughtry, C.S.T.; Walthall, C.L.; Kim, M.S.; De Colstoun, E.B.; McMurtrey, J.E. Estimating Corn Leaf Chlorophyll Concentration from Leaf and Canopy Reflectance. *Remote Sens. Environ.* **2000**, *74*, 229–239. [CrossRef]
45. Haboudane, D.; Miller, J.R.; Tremblay, N.; Zarco-Tejada, P.J.; Dextraze, L. Integrated Narrow-Band Vegetation Indices for Prediction of Crop Chlorophyll Content for Application to Precision Agriculture. *Remote Sens. Environ.* **2002**, *81*, 416–426. [CrossRef]
46. Gitelson, A.A.; Kaufman, Y.J.; Merzlyak, M.N.; Blaustein, J. Use of a Green Channel in Remote Sensing of Global Vegetation from EOS-MODIS. *Remote Sens. Environ.* **1995**, *58*, 289–298. [CrossRef]
47. Gitelson, A.A.; Viña, A.; Ciganda, V.; Rundquist, D.C.; Arkebauer, T.J. Remote Estimation of Canopy Chlorophyll Content in Crops. *Geophys. Res. Lett.* **2005**, *32*, 1–4. [CrossRef]
48. Jiang, Z.; Huete, A.R.; Didan, K.; Miura, T. Development of a Two-Band Enhanced Vegetation Index Without a Blue Band. *Remote Sens. Environ.* **2008**, *112*, 3833–3845. [CrossRef]
49. Cao, Q.; Miao, Y.; Feng, G.; Gao, X.; Li, F.; Liu, B.; Yue, S.; Cheng, S.; Ustin, S.L.; Khosla, R. Active Canopy Sensing of Winter Wheat Nitrogen Status: An Evaluation of Two Sensor Systems. *Comput. Electron. Agric.* **2015**, *112*, 54–67. [CrossRef]
50. Haboudane, D.; Miller, J.R.; Pattey, E.; Zarco-Tejada, P.J.; Strachan, I.B. Hyperspectral Vegetation Indices and Novel Algorithms for Predicting Green LAI of Crop Canopies: Modeling and Validation in the Context of Precision Agriculture. *Remote Sens. Environ.* **2004**, *90*, 337–352. [CrossRef]
51. Huete, A.R. A Soil-Adjusted Vegetation Index (SAVI). *Remote Sens. Environ.* **1988**, *25*, 295–309. [CrossRef]

52. Penuelas, J.; Frederic, B.; Filella, I. Semi-Empirical Indices to Assess Carotenoids/Chlorophyll-a Ratio from Leaf Spectral Reflectance Diversity and Ecosystem Functions of Boreal Forest under Global Change View Project Vegetation Indices. *Photosynthetica* **1995**, *31*, 221–230. [CrossRef]
53. Cao, Q.; Miao, Y.; Wang, H.; Huang, S.; Cheng, S.; Khosla, R.; Jiang, R. Non-Destructive Estimation of Rice Plant Nitrogen Status with Crop Circle Multispectral Active Canopy Sensor. *Field Crops Res.* **2013**, *154*, 133–144. [CrossRef]
54. Raper, T.B.; Varco, J.J. Canopy-Scale Wavelength and Vegetative Index Sensitivities to Cotton Growth Parameters and Nitrogen Status. *Precis. Agric.* **2015**, *16*, 62–76. [CrossRef]
55. Maes, W.H.; Steppe, K. Estimating Evapotranspiration and Drought Stress with Ground-Based Thermal Remote Sensing in Agriculture: A Review. *J. Exp. Bot.* **2012**, *63*, 4671–4712. [CrossRef]
56. Maes, W.H.; Huete, A.R.; Steppe, K. Optimizing the Processing of UAV-Based Thermal Imagery. *Remote Sens.* **2017**, *9*, 476. [CrossRef]
57. Jiang, J.; Atkinson, P.M.; Zhang, J.; Lu, R.; Zhou, Y.; Cao, Q.; Tian, Y.; Zhu, Y.; Cao, W.; Liu, X. Combining Fixed-Wing UAV Multispectral Imagery and Machine Learning to Diagnose Winter Wheat Nitrogen Status at the Farm Scale. *Eur. J. Agron.* **2022**, *138*, 126537. [CrossRef]
58. Yue, S.; Meng, Q.; Zhao, R.; Li, F.; Chen, X.; Zhang, F.; Cui, Z. Critical Nitrogen Dilution Curve for Optimizing Nitrogen Management of Winter Wheat Production in the North China Plain. *Agron. J.* **2012**, *104*, 523–529. [CrossRef]
59. Sellami, M.H.; Albrizio, R.; Čolović, M.; Hamze, M.; Cantore, V.; Todorovic, M.; Piscitelli, L.; Stellacci, A.M. Selection of Hyperspectral Vegetation Indices for Monitoring Yield and Physiological Response in Sweet Maize under Different Water and Nitrogen Availability. *Agronomy* **2022**, *12*, 489. [CrossRef]
60. Taşan, S.; Cemek, B.; Taşan, M.; Cantürk, A. Estimation of Eggplant Yield with Machine Learning Methods Using Spectral Vegetation Indices. *Comput. Electron. Agric.* **2022**, *202*, 107367. [CrossRef]
61. López del Val, J.A.; Alonso Pérez de Agreda, J.P. Principal Components Analysis. *Aten. Primaria/Soc. Española De Med. De Fam. Y Comunitaria* **1993**, *12*, 333–338. [CrossRef]
62. Chen, T.; Guestrin, C. XGBoost: A Scalable Tree Boosting System. In Proceedings of the ACM SIGKDD International Conference on Knowledge Discovery and Data Minin, San Francisco, CA, USA, 13–17 August 2016; Association for Computing Machinery: New York, NY, USA, 2016; pp. 785–794. [CrossRef]
63. Chlingaryan, A.; Sukkarieh, S.; Whelan, B. Machine learning approaches for crop yield prediction and nitrogen status estimation in precision agriculture: A review. *Comput. Electron. Agric.* **2018**, *151*, 61–69. [CrossRef]
64. Neuhaus, A.; Sadras, V.O. Relationship between Rainfall-Adjusted Nitrogen Nutrition Index and Yield of Wheat in Western Australia. *J. Plant Nutr.* **2018**, *41*, 2637–2643. [CrossRef]
65. Szczepaniak, W.; Potarzycki, J. Impact of Increasing Nitrogen Rates on the Course of the Nitrogen Critical Concentration Curve During the Vegetative Growth of Winter Wheat. *J. Elem.* **2014**, *19*, 549–566. [CrossRef]
66. Hoogmoed, M.; Neuhaus, A.; Noack, S.; Sadras, V.O. Benchmarking Wheat Yield Against Crop Nitrogen Status. *Field Crops Res.* **2018**, *222*, 153–163. [CrossRef]
67. Kunrath, T.R.; Lemaire, G.; Sadras, V.O.; Gastal, F. Water Use Efficiency in Perennial Forage Species: Interactions Between Nitrogen Nutrition and Water Deficit. *Field Crops Res.* **2018**, *222*, 1–11. [CrossRef]
68. Duncan, E.G.; O'Sullivan, C.A.; Roper, M.M.; Palta, J.; Whisson, K.; Peoples, M.B. Yield and Nitrogen Use Efficiency of Wheat Increased with Root Length and Biomass Due to Nitrogen, Phosphorus, and Potassium Interactions. *J. Plant Nutr. Soil Sci.* **2018**, *181*, 364–373. [CrossRef]
69. Berger, K.; Machwitz, M.; Kycko, M.; Kefauver, S.C.; Van Wittenberghe, S.; Gerhards, M.; Verrelst, J.; Atzberger, C.; van der Tol, C.; Damm, A.; et al. Multi-Sensor Spectral Synergies for Crop Stress Detection and Monitoring in the Optical Domain: A Review. *Remote Sens. Environ.* **2022**, *280*, 113198. [CrossRef] [PubMed]
70. Goel, P.K.; Prasher, S.O.; Landry, J.A.; Patel, R.M.; Bonnell, R.B.; Viau, A.A.; Miller, J.R. Potential of Airborne Hyperspectral Remote Sensing to Detect Nitrogen Deficiency and Weed Infestation in Corn. *Comput. Electron. Agric.* **2003**, *38*, 99–124. [CrossRef]
71. Feng, Z.; Guan, H.; Yang, T.; He, L.; Duan, J.; Song, L.; Wang, C.; Feng, W. Estimating the Canopy Chlorophyll Content of Winter Wheat Under Nitrogen Deficiency and Powdery Mildew Stress Using Machine Learning. *Comput. Electron. Agric.* **2023**, *211*, 107989. [CrossRef]
72. Zhang, J.; Qiu, X.; Wu, Y.; Zhu, Y.; Cao, Q.; Liu, X.; Cao, W. Combining Texture, Color, and Vegetation Indices from Fixed-Wing UAS Imagery to Estimate Wheat Growth Parameters Using Multivariate Regression Methods. *Comput. Electron. Agric.* **2021**, *185*, 106138. [CrossRef]
73. Pei, S.; Dai, Y.; Bai, Z.; Li, Z.; Zhang, F.; Yin, F.; Fan, J. Improved Estimation of Canopy Water Status in Cotton Using Vegetation Indices along with Textural Information from UAV-Based Multispectral Images. *Comput. Electron. Agric.* **2024**, *224*, 109176. [CrossRef]
74. Tilling, A.K.; O'Leary, G.J.; Ferwerda, J.G.; Jones, S.D.; Fitzgerald, G.J.; Rodriguez, D.; Belford, R. Remote Sensing of Nitrogen and Water Stress in Wheat. *Field Crops Res.* **2007**, *104*, 77–85. [CrossRef]

75. Yang, D.Q.; Dong, W.H.; Luo, Y.L.; Song, W.T.; Cai, T.; Li, Y.; Yin, Y.P.; Wang, Z.L. Effects of Nitrogen Application and Supplemental Irrigation on Canopy Temperature and Photosynthetic Characteristics in Winter Wheat. *J. Agric. Sci.* **2018**, *156*, 13–23. [CrossRef]
76. Nielsen, D.C.; Halvorson, A.D. Nitrogen Fertility Influence on Water Stress and Yield of Winter Wheat. *Agron. J.* **1991**, *83*, 1065–1070. [CrossRef]
77. Liu, Y.; Hatou, K.; Aihara, T.; Kurose, S.; Akiyama, T.; Kohno, Y.; Lu, S.; Omasa, K. A Robust Vegetation Index Based on Different UAV RGB Images to Estimate SPAD Values of Naked Barley Leaves. *Remote Sens.* **2021**, *13*, 686. [CrossRef]
78. Zhang, Y.; Xia, C.; Zhang, X.; Cheng, X.; Feng, G.; Wang, Y.; Gao, Q. Estimating the Maize Biomass by Crop Height and Narrowband Vegetation Indices Derived from UAV-Based Hyperspectral Images. *Ecol. Indic.* **2021**, *129*, 107985. [CrossRef]
79. Zhang, J.; Cheng, T.; Guo, W.; Xu, X.; Qiao, H.; Xie, Y.; Ma, X. Leaf Area Index Estimation Model for UAV Image Hyperspectral Data Based on Wavelength Variable Selection and Machine Learning Methods. *Plant Methods* **2021**, *17*, 49. [CrossRef] [PubMed]
80. Kulpanich, N.; Worachairungreung, M.; Thanakunwutthirot, K.; Chaiboonrueang, P. The Application of Unmanned Aerial Vehicles (UAVs) and Extreme Gradient Boosting (XGBoost) to Crop Yield Estimation: A Case Study of Don Tum District, Nakhon Pathom, Thailand. *Int. J. Geoinform.* **2023**, *19*, 65–77. [CrossRef]

Disclaimer/Publisher's Note: The statements, opinions and data contained in all publications are solely those of the individual author(s) and contributor(s) and not of MDPI and/or the editor(s). MDPI and/or the editor(s) disclaim responsibility for any injury to people or property resulting from any ideas, methods, instructions or products referred to in the content.